

In Situ and Radar Observations of the Low Reflectivity Ribbon in Supercells during VORTEX2

CASEY B. GRIFFIN,^{a,b,c} CHRISTOPHER C. WEISS,^a ANTHONY E. REINHART,^{a,d} JEFFREY C. SNYDER,^d
HOWARD B. BLUESTEIN,^b JOSHUA WURMAN,^c AND KAREN A. KOSIBA^c

^a *Texas Tech University, Lubbock, Texas*

^b *School of Meteorology, University of Oklahoma, Norman, Oklahoma*

^c *Advanced Radar Research Center, University of Oklahoma, Norman, Oklahoma*

^d *Cooperative Institute for Mesoscale Meteorological Studies, University of Oklahoma, and
NOAA/OAR/National Severe Storms Laboratory, Norman, Oklahoma*

^e *Center for Severe Weather Research, Boulder, Colorado*

(Manuscript received 12 July 2017, in final form 17 November 2017)

ABSTRACT


During the second Verification of the Origins of Rotation in Tornadoes Experiment (VORTEX2) field campaign, mobile radars observed a previously undocumented feature: the low-reflectivity ribbon (LRR). The LRR was characterized by reduced reflectivity Z_H and differential reflectivity Z_{DR} through a narrow region extending from the intersection of the hook and forward-flank regions of supercells. This study synthesizes kinematic and polarimetric radar observations with in situ measurements taken by the “StickNet” observing network. StickNet data have been used to establish that the LRR is associated with a localized minimum in pseudoequivalent potential temperature θ_{ep} . Pronounced drops in θ_{ep} are observed by nine separate probes in three different supercell thunderstorms. Both single- and dual-Doppler analyses are used to examine the two- and three-dimensional structures of the winds within the LRR, revealing that the LRR is associated with cyclonic vertical vorticity aloft. Polarimetric radar observations are used to study the hydrometeor characteristics and the processes that cause those hydrometers to be present. Special consideration is given to the analysis of the vertical distribution of traditional and polarimetric variables, as well as the evolution of the kinematic fields retrieved by dual-Doppler analysis. The combination of thermodynamic, kinematic, and inferred microphysical observations supports a hypothesis that the LRR comprises sparse, large hail.

1. Introduction

The second Verification of the Origins of Rotation in Tornadoes Experiment (VORTEX2) (Wurman et al. 2012) occurred in the spring seasons of 2009 and 2010. A primary objective was to obtain simultaneous wind, precipitation, and thermodynamic data to better understand the processes that differentiate nontornadic supercells from weakly tornadic and violently tornadic supercells. The project was successful in documenting the pretornadic (Markowski et al. 2012a,b), tornado-genesis (Kosiba et al. 2013), and tornado maintenance

(Marquis et al. 2014, 2016) phases of a tornadic supercell with unprecedented spatial and temporal resolutions. During VORTEX2, the Doppler on Wheels (DOW) (Wurman et al. 1997; Wurman 2001) and University of Massachusetts (UMass) X-Pol (Junyent-Lopez 2003) mobile polarimetric radars (Table 1) were the first to document a feature called the low reflectivity ribbon (LRR).

Wurman et al. (2012), Kosiba et al. (2013), and Snyder et al. (2013) describe the LRR as a narrow band of locally reduced reflectivity Z_H and differential reflectivity Z_{DR} extending from where the hook echo intersects the main body of the storm near the rear of the forward-flank reflectivity echo (Fig. 1). Kosiba et al. (2013) note that the LRR often extends through a deep region of a supercell, apparently bisecting it on occasion, and describe its appearance near the time of tornadogenesis, filling as the tornado intensified. The typical deficit in Z_H is 5–15 dBZ; however, local deficits

 Denotes content that is immediately available upon publication as open access.

Corresponding author: Casey B. Griffin, casey.griffin@ou.edu

TABLE 1. A selection of radar characteristics of the DOW and UMass X-Pol radar platforms.

Radar characteristic	DOW6	DOW7	UMass X-Pol
Operating frequency 1	9.40 GHz	9.35 GHz	9.41 GHz
Operating frequency 2	9.55 GHz	9.50 GHz	—
Peak power	250/500 kW (2009/10)	250/500 kW (2009/10)	12.5 kW
Pulse width	200–2000 ns (400 ns)	200–2000 ns (400 ns)	Typically 1 μ s
PRF	Up to 5000 Hz	Up to 5000 Hz	1.6 and 2.0 kHz
Antenna diameter	2.44 m	2.44 m	1.8 m
Half-power beamwidth	0.93°	0.93°	1.25°
Peak scanning rate	50° s ⁻¹	50° s ⁻¹	24° s ⁻¹
Gate length	As low as 30 m	As low as 30 m	Typically 150 m
Polarimetric diversity during VORTEX2 (years)	2010 only	2010 only	2009–10

exceed 20 dBZ in some cases (Wurman et al. 2012; Kosiba et al. 2013; Snyder et al. 2013). The typical value of Z_{DR} within the LRR at X-band is approximately 0–2 dB, yielding relative deficits of 2–5 dB, compared to surrounding areas. The LRR also occasionally appears in the correlation coefficient ρ_{hv} and differential phase Φ_{DP} (Snyder et al. 2013). The representation of the LRR in ρ_{hv} and Φ_{DP} is inconsistent from case to case, and thus, it is not possible to identify a typical range of values. Its width usually ranges from \sim 300 m to \sim 1 km, and it is often most evident below 2.5–3.0 km (Snyder et al. 2013).

While previous studies have documented the polarimetric and some of the kinematic characteristics of the LRR, no work has been done to investigate its thermodynamic properties. Documenting the thermodynamic properties of the LRR is particularly important

for understanding whether the LRR locally impacts buoyancy or generates vorticity through baroclinity. Baroclinic vorticity generation in the core of the supercell and its role in tornadogenesis and near-surface mesocyclogenesis has been a topic of recent interest (e.g., Dahl et al. 2014). Additionally, the relative buoyancy of parcels traversing and originating in vorticity source regions can have an impact on the tornadic potential of a storm (Markowski et al. 2002).

This study investigates the thermodynamic characteristics of LRRs associated with the 5 June 2009, 18 May 2010, and 10 June 2010 supercells from the VORTEX2 campaign. Dual-Doppler and polarimetric analyses from the 5 June 2009 Goshen County, Wyoming, supercell are also presented, with the purpose of documenting the evolution of the LRR and some of the kinematic processes that occur near the ribbon.

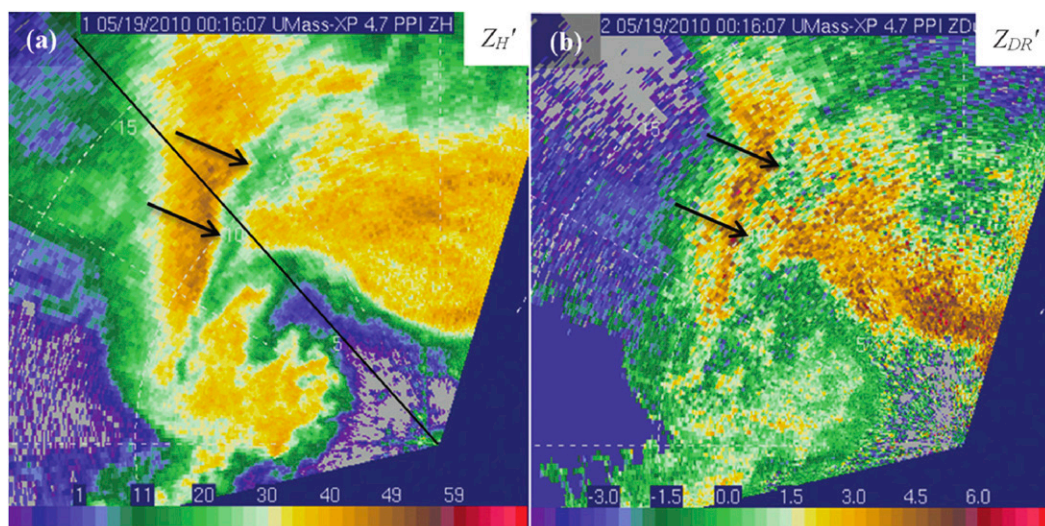


FIG. 1. PPI displays of (a) reflectivity (dBZ) and (b) differential reflectivity (dB) observations that illustrate an LRR in an 18 May 2010 tornadic supercell, adapted from Snyder et al. (2013). Arrows indicate the position of the LRR in each panel, and the black line in (a) represents a cross section presented in Snyder et al. (2013).

2. Methods

a. Thermodynamic data analysis

Surface measurements of pressure, temperature, wind speed, wind direction, and relative humidity were collected during VORTEX2 by a suite of mobile, 2.5-m tall “StickNet” observing platforms that were developed by Texas Tech University’s Atmospheric Science Group and the National Wind Institute (Weiss and Schroeder 2008; Schroeder and Weiss 2008; Weiss et al. 2015). GPS positions and deployment times of the StickNet probes were overlaid with radar data from all the VORTEX2 cases to determine instances when surface data were collected concurrently with the passing of the LRR over the probes. This study uses data from nine probes collected in three separate cases. Time series of state and calculated variables are compared to radar data to determine whether any notable changes are observed consistently with the passing of LRRs.

Pseudoequivalent potential temperature θ_{ep} is calculated using the equation derived by Bolton (1980). Thermodynamic observations can be expanded into a two-dimensional horizontal plane using a time-to-space conversion under a steady-state assumption (Taylor 1938). Although the Taylor hypothesis is difficult to justify for supercells because of their rapid evolution, previous studies have been successful in assuming a steady state for short time periods on the order of 5–10 min (e.g., Markowski et al. 2002; Skinner et al. 2011, 2014). Time windows of ~15 min are used in this study. Slightly longer time windows are used to fully resolve the spatial extent of the LRR, especially when the LRR is oriented in the east–west direction, perpendicular to the array of StickNet probes (which are usually aligned north–south). The analyses are temporally centered on the approximate time that the LRR passes over the array, effectively minimizing the restrictiveness of the steady-state assumption in the region of interest, especially for instances when the LRR is largely parallel to the array.¹ Time-to-space conversions are only performed for the 18 May 2010 Dumas, Texas, case. Storm motion for this case is calculated using the radar-indicated position of the intersection between the rear-flank gust front (RFGF) and forward-flank reflectivity gradient (FFRG) over the period of 2300–0100 UTC, as described by Skinner et al. (2011) and Weiss et al. (2015).

¹ Recall, the steady-state assumption decreases linearly toward the center of the analysis window; thus, for an instance where the LRR is parallel to the array, the LRR is only assumed to be steady state for ~1–2 min while it passes over the array.

Time-to-space converted data are gridded and interpolated onto a two-dimensional plane using a two-pass Barnes objective analysis scheme (Barnes 1964). Because the time-to-space converted variables have much greater spatial resolution tangential to supercell motion, only every 60th observation (~10 m) is included in the objective analysis. A Barnes weighting function w_b is used (Trapp and Doswell 2000):

$$w_b = \exp\left(\frac{-t^2}{\kappa_t} - \frac{n^2}{\kappa_n}\right), \quad (1)$$

where t and n are the tangential and normal distances, respectively, relative to storm motion from the current grid point to the data point. The maximum radius of influence for each observation is 10 km to ensure proper sampling of stations spaced an average distance of 4.2 km apart (Weiss et al. 2015). The variables κ_t and κ_n are the smoothing parameters that are tangential and normal to the storm motion, as described by Koch et al. (1983):

$$\kappa = 5.052 \left(\frac{2\Delta n}{\pi}\right)^2, \quad (2)$$

where Δn is the mean spacing between observations, a constant. Analyses use a grid spacing of 300 m. The second-pass convergence parameter γ of 0.1 is used in Barnes (1973)’s Eqs. (11)–(14) to further recover the amplitudes of the major wavelengths. Gridded data are plotted over radar data collected nearest the center of the window for which time-to-space data are computed. The time-to-space converted data allow a spatial comparison to be made between the positions of the LRR and θ_{ep} to supplement the temporal comparison illustrated by the time series.

b. Radar data processing

Quality control of the radar data utilized the National Center for Atmospheric Research (NCAR) Earth Observing Laboratory (EOL)’s Solo II editing software and the Doppler Radar Data Exchange Format (DORADE) Radar Editing Algorithms, Detection, Extraction, and Retrieval (DREADER) software created by Curtis Alexander [NOAA/Earth System Research Laboratory (ESRL)]. Data are plotted in plan position indicator (PPI) and constant altitude PPI (CAPPI) format, allowing for the best illustration of the deficits in Z_H , Z_{DR} , and ρ_{hv} observed within the LRR. To subset data within the LRR, the boundary of the LRR is drawn using the maximum horizontal gradient in Z_H to guide the selection of the edges inside the precipitation core (Fig. 2). The FFRG is used to define the

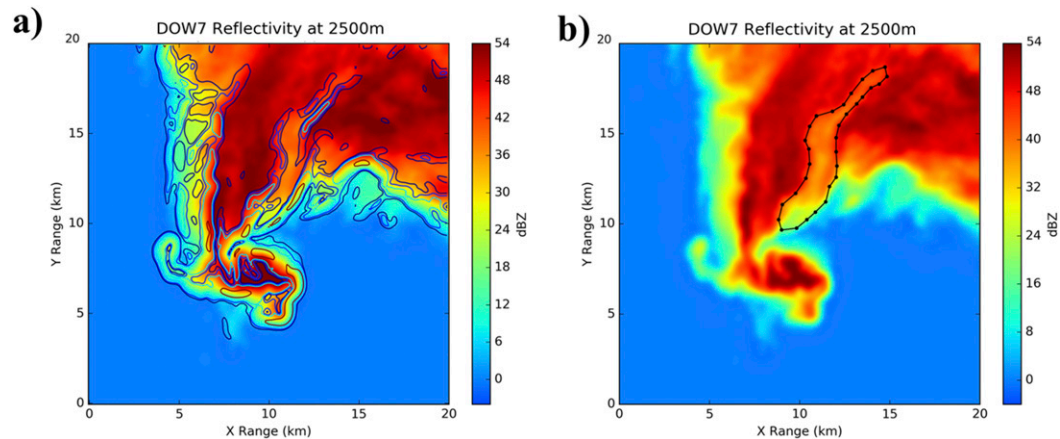


FIG. 2. Horizontal cross sections at 2500 m showing objectively analyzed reflectivity (shaded; dBZ) with (a) reflectivity gradient (contoured every $6 \times 10^{-3} \text{ dBZ m}^{-1}$) and (b) the bound region (black) containing the LRR. Data were collected by DOW7 at 2150 UTC 5 Jun 2009 in southeastern WY.

southern boundary of the LRR. In some instances, only Z_{DR}^2 is used to illustrate the location of the LRR. In these instances, the deficit in Z_{DR} is more pronounced than the deficit in Z_{H} , or the deficit in Z_{H} was filtered out by the objective analysis, as is the case in the Dumas dataset. However, please note that there is an associated, if less easily identifiable, deficit in Z_{H} in every instance where only Z_{DR} is shown.

Radial plots of polarimetric variables are used for the analysis of cumulative fields (e.g., Φ_{DP}). Because of the noisy nature of Φ_{DP} , a 300-m moving average is used to smooth the data and better isolate signals of interest. PPIs and radial plots that are not gridded output from objective analyses are visualized using Solo II and the Python Atmospheric Radiation Measurement (ARM) Radar Toolkit (Py-ART) module developed by the Department of Energy ARM Climate Research Facility (Helmus and Collis 2016).

c. Dual-Doppler analysis

Objective and dual-Doppler analyses of radar data are created from the 5 June 2009 Goshen County, Wyoming, dataset using the Observation Processing and Wind Synthesis (OPAWS) code (<http://code.google.com/p/opaws/>)

² Absolute calibration for the radars was done in the field by injecting signals of known intensity into the receivers, and Z_{DR} calibration was performed using vertically pointing scans in light rain; however, calibration was likely not performed frequently enough to avoid some error. Additionally, Z_{DR} data used for this project are not corrected for attenuation or differential attenuation; however, the LRR is represented by a relative minimum in these fields, and thus, it can be easily identified without the implementation of any corrections.

developed by David Dowell (NOAA/ESRL) and Lou Wicker (National Severe Storms Laboratory). DOW radar data are objectively analyzed using a two-pass Barnes technique (Barnes 1964; Majcen et al. 2008) with a second-pass convergence parameter γ of 0.3. For a half-power beamwidth of 0.9° and an elevation interval of 1° at an average range of 20 km, the horizontal and vertical smoothing parameter κ is 0.216 km. These parameters follow the Kosiba et al. (2013) dual-Doppler analyses of the Goshen supercell, which used the same DOW6 and DOW7 data analyzed for this study. Radar data are objectively analyzed on a $30 \text{ km} \times 30 \text{ km}$ horizontal domain. Horizontal grid spacing of 100 m and vertical grid spacing of 250 m are chosen for the analysis.

Dual-Doppler wind syntheses are calculated in regions where the look angle differences between the radars are between 20° and 160° using upward integration. Vertical velocities are calculated using the traditional upward integration of the mass continuity equation. Lower boundary conditions of $w = 0$ at $z = 0$ are used. Density is assumed to decrease exponentially with height. Hydrometeor fall speeds are corrected for using the terminal fall velocity–reflectivity relationships obtained from Joss and Waldvogel (1970). Uncertainties arise in the lowest analysis levels due to poor radar coverage near the ground, and thus, the analyses at the lowest altitudes are excluded. Translation of the 5 June 2009, Goshen County, Wyoming, supercell between each radar sweep in a volume is corrected for using a constant translation velocity of $(u, v) = (10.6, -2.8) \text{ m s}^{-1}$ as in Kosiba et al. (2013), which was determined using the DOW-measured low-level mesocyclone locations from 2143 to 2203 UTC.

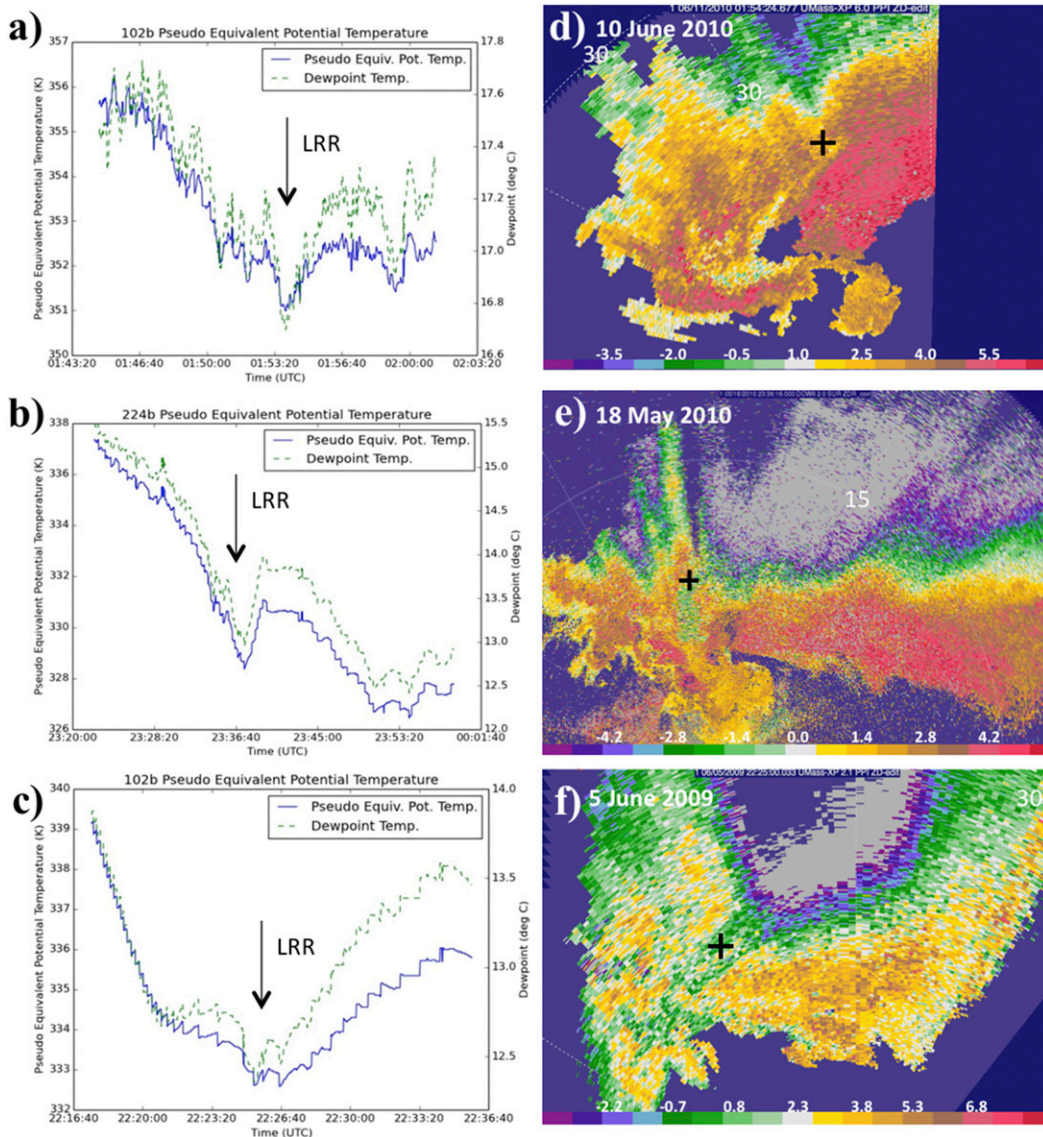


FIG. 3. Comparison of (a)–(c) time series of θ_{ep} (blue trace; K) and Td (green trace; °C) and (d)–(f) StickNet positions (plus signs) relative to the representation of the LRR in differential reflectivity (dB) on (a),(d) 10 Jun 2010; (b),(e) 18 May 2010; and (c),(f) 5 Jun 2009. Radar data are from (d),(f) UMass X-Pol and (e) DOW6 respectively. Reference ranges (km) in (d)–(f) are labeled in white.

3. Results

a. Thermodynamic analyses

1) TIME SERIES

Nine separate probes directly sampled the LRR in the three cases interrogated in this study. All nine probes observe a distinct minimum in θ_{ep} with the passing of the LRR. A representative probe from each of the three cases is shown in Fig. 3. The comparison of thermodynamic time series data with the mobile radar-indicated position of the LRR in the 10 June 2010 Last Chance, Colorado (Fig. 3d),

18 May 2010 Dumas, Texas (Fig. 3e), and 5 June 2009 Goshen County, Wyoming (Fig. 3f), supercells reveal that the passing of the LRR coincides closely with localized minima in θ_{ep} at the surface (Figs. 3a–c). Lower values of θ_{ep} were measured later in each of the StickNet deployments; however, the LRR exhibits a local minimum within a large-scale decreasing trend in θ_{ep} associated with the cold pool. The minimum in θ_{ep} is associated with a local minimum in temperature (Fig. 4a) and dewpoint temperature T_d (Fig. 4b), coinciding with the passing of the LRR. The peak in pressure measured at the surface in Fig. 4c appears to be on the storm scale rather than on the scale of the LRR.

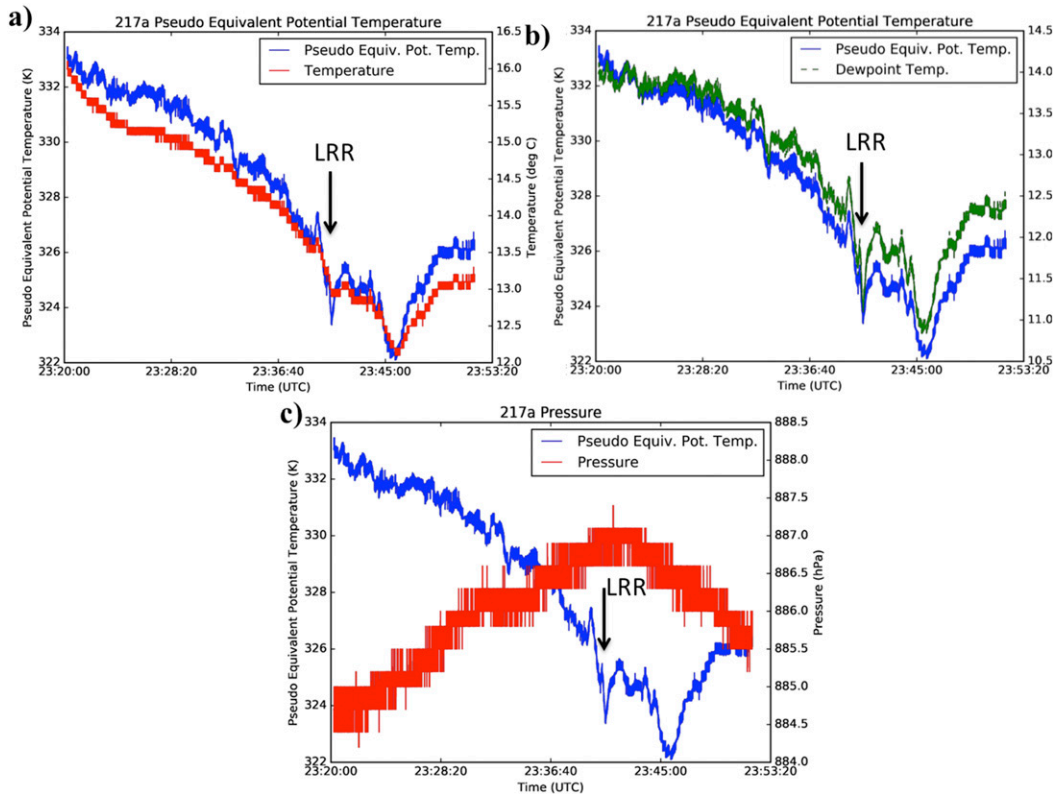


FIG. 4. Time series of θ_{ep} (blue trace; K) and (a) temperature (red trace; °C), (b) Td (green trace; °C), and (c) pressure (red trace; hPa) collected by StickNet probe 217a on 18 May 2010 that illustrate that the deficit in θ_{ep} most closely corresponds with a minimum in dewpoint temperature.

An illustrative StickNet dataset was collected by probe 213a on 18 May 2010. Probe 213a samples at least two separate LRRs (Fig. 5); the first, a largely east–west-oriented LRR, is sampled at 2328 UTC (Fig. 5a) when two LRRs were occurring simultaneously. The first LRR quickly dissipates in its DOW6 representation, while the second, a north–south-oriented LRR, persists and is sampled by an array of five probes, including probe 213a at approximately 2336 UTC (Fig. 6). A third local minimum in θ_{ep} is observed by the array at 2340 UTC, but a potential third LRR cannot be positively identified owing to attenuation.

2) TIME-TO-SPACE CONVERSION OF THE 10 MAY 2010 DUMAS, TEXAS, SUPERCELL

The radar-indicated positions of LRRs are compared with the minima in θ_{ep} using time-to-space conversion of observed thermodynamic data from particularly well-sampled LRRs.³

³ Only the 18 May 2010 Dumas, Texas, LRRs were sampled by more than two StickNet probes, and thus, time-to-space analyses are only performed on this case. For a complete description and visualization of the 18 May 2010 StickNet deployment, see Weiss et al. (2015).

A time-to-space conversion of 12 probes using 16 min of data centered on the 2328 UTC position of the LRR (Fig. 7) illustrates that a minimum in θ_{ep} (centered on the dashed line) is spatially collocated with the 0-dB Z_{DR} contour, which approximately marks the outer boundary of the LRR.⁴ A later time-to-space analysis using the same probes illustrates a period when the LRR had a more north–south orientation and was directly sampled by five StickNet probes (Fig. 8). The LRR again appears as a minimum in θ_{ep} in this analysis. This minimum is apparent through the center of the southern portion of the LRR and also can be seen, to a lesser extent, in the northern part of the ribbon.

The impact of the thermodynamic characteristics associated with LRRs is currently not understood; it is not known whether they modulate supercell behavior, or if they are just finescale features produced as a result of precipitation processes. For example, the localized deficit in θ_{ep} may reduce parcel buoyancy near the LRR and alter the vertical velocity tendency. Additionally, the gradient in θ_{ep} near the

⁴ The θ_{ep} analyses presented in Figs. 8 and 9 are given in relation to a base-state value of 340.77 K, which was the StickNet probe average temperature at 2305 UTC prior to interacting with the storm.

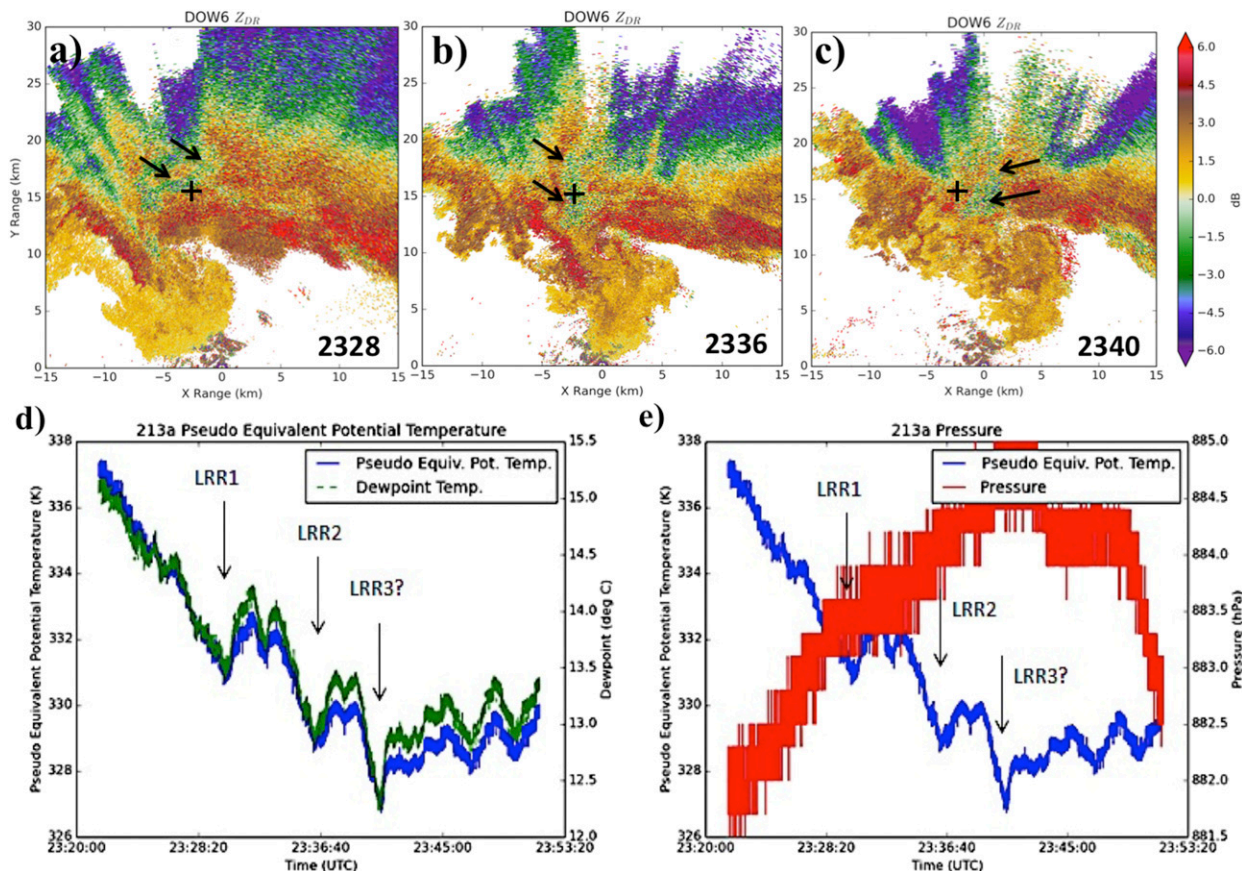


FIG. 5. (a)–(c) Comparison of the position of StickNet probe 213a relative to the manifestation of the LRR in differential reflectivity (dB) from DOW6 on 18 May 2010, and time series of θ_{ep} (blue trace; K) with (d) Td (green trace; °C) and (e) pressure (red trace; hPa) taken by StickNet probe 213a. A possible third LRR cannot be ruled out, but attenuation and differential attenuation prevents its presence from being confirmed.

LRR may have an impact on the local vorticity budget through baroclinity. Further understanding of any tornado- or mesocyclone-bound parcel interaction with the LRR is vital to studies of supercell and tornado dynamics but is left for future work (i.e., additional observations or simulations).

b. Dual-Doppler observations from the 9 June 2009 Goshen County, Wyoming, supercell

1) KINEMATIC RESULTS

Dual-Doppler analyses are performed for the 9 June 2009 Goshen County, Wyoming, supercell. While dual-Doppler coverage is available for the 18 May 2010 Dumas, Texas, case, the coverage of sufficient look angle difference for dual-Doppler is shallow near the LRR, and thus, analyses are not presented.⁵ In the lowest 2 km above radar level

(ARL) (all altitudes henceforth are in ARL), the Goshen County, Wyoming, LRR exhibits no temporally consistent kinematic properties. This is consistent with what was previously noted in Kosiba et al. (2013). Above approximately 2–2.5 km, it is seen that mature LRRs (e.g., Figs. 9a,b) are often found in downdrafts (Fig. 9d). However, developing LRRs are often found in regions dominated by upward vertical velocity (Fig. 9c). Thus, the direction of vertical motion within the LRR may be life cycle dependent, which will be further discussed in section 4b.

The calculated vertical vorticity ζ is rather noisy aloft (not shown). However, the mean value of ζ at all altitudes above 2 km is decidedly positive within the LRR [and the distribution of ζ near-normal (not shown)] at all times prior to its decay. This will be a topic of discussion in the next section.

2) EVOLUTION OF THE LRR

At 2142 UTC, the supercell has a mature LRR (denoted as LRR A) and a developing LRR (denoted as LRR B)

⁵No dual-Doppler data were available for the Last Chance, Colorado, supercell while it was producing an LRR.

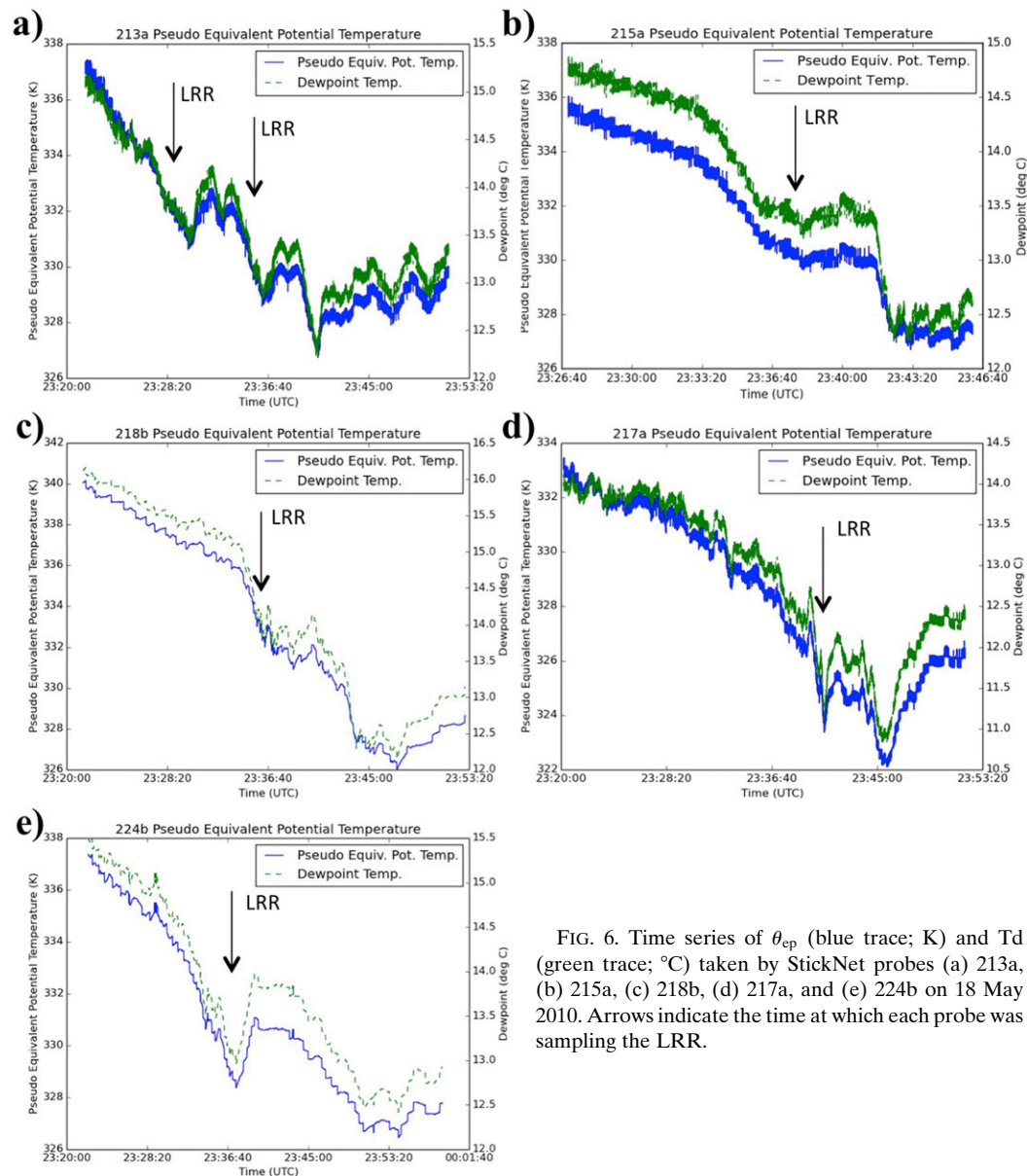


FIG. 6. Time series of θ_{ep} (blue trace; K) and T_d (green trace; °C) taken by StickNet probes (a) 213a, (b) 215a, (c) 218b, (d) 217a, and (e) 224b on 18 May 2010. Arrows indicate the time at which each probe was sampling the LRR.

that manifests as a notch along the FFRG (Fig. 10a). By 2144 UTC, LRR A exhibits greater reflectivity, whereas LRR B now appears as a region of locally reduced Z_H that extends into the main precipitation core (Fig. 10b). Developing LRR C now manifests as a notch along the FFRG, similar to LRR B at the 2142 UTC. At 2146 UTC, LRR A exhibits an increase in Z_H and enters what will be called the “decay” stage of its life cycle (Fig. 10c). LRR B exhibits a well-defined, elongated region of reduced Z_H , a trait that characterizes what will be called the “mature” stage of the LRR life cycle. Developing LRR C still exists as a notch along the FFRG.

By 2148 UTC, developing LRR C is now an elongated notch in the FFRG (Fig. 10d). LRR B has translated toward the rear flank of the supercell and is more north-south-oriented, compared to the previous times. LRR A, which is difficult to identify, has largely decayed. By 2150 UTC, LRR B exhibits greater reflectivity and has narrowed considerably (Figs. 10e). Maturing LRR C is slightly more elongated than it was at previous times. LRR D, a developing ribbon, appears as a notch along the FFRG. At 2152 UTC, LRR B continues to fill, and LRR C exhibits greater Z_H than at 2150 UTC (Fig. 10e). Developing LRR D now exhibits very little deficit in Z_H

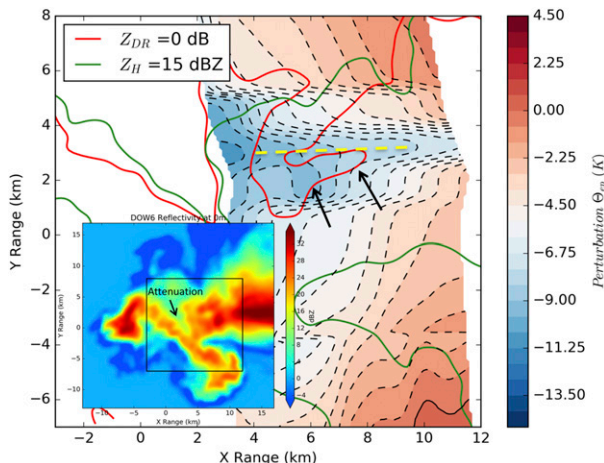


FIG. 7. Objectively analyzed time-to-space conversion of perturbation θ_{ep} (shaded; K) from the array of StickNet probes deployed near Dumas, TX, on 18 May 2010. Overlaid on the plot are the 0-dB differential reflectivity (red) and 15-dBZ reflectivity (green) contours valid at 2328 UTC. Inset is dBZ from DOW6 at 2328 UTC overlaid with a box outlining the enlarged area. The arrows indicate the positions of the LRR. The dashed yellow line indicates the local minimum in θ_{ep} . The analysis uses 16 min of data centered on 2328 UTC.

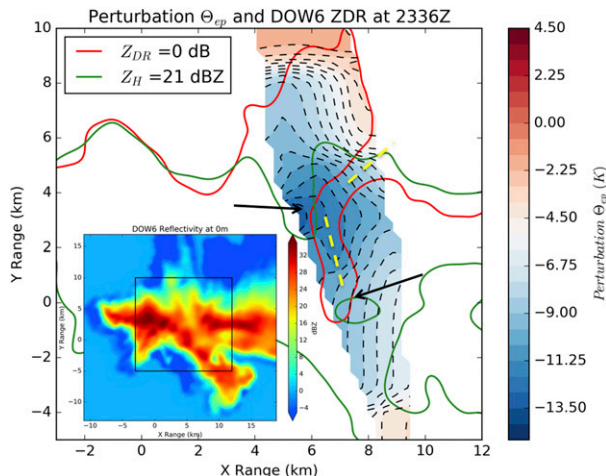


FIG. 8. As in Fig. 7, but the analysis period centers on 2336 UTC, uses 12 min of data, and has a 21-dBZ reflectivity overlay.

but has transformed into a small, ribbonlike feature that resembles a smaller version of LRRs B and C. All three ribbons curve from west to east and are largely parallel to one another.

The formation of a notch along the FFRG, and the elongation of this notch into a ribbon, likely involves the deformation of the Z_H field near the LRR.⁶ From the previous discussion, it is clear that LRR C exemplifies the maturation of a ribbon (Fig. 11). At 2148 UTC, locally enhanced deformation is observed within developing LRR C (Fig. 11a). The local axes of dilatation,⁷ denoted by the vectors, are largely parallel with the axis of the Z_H notch in the southern part of the ribbon. At 2150 UTC, the axes of dilatation are parallel to LRR C throughout the entire region of reduced reflectivity, and LRR C has become elongated in the direction of stretching (Fig. 11b). In addition, a notch in Z_H has developed (LRR D) and exhibits an axis largely parallel to the local axes of dilatation. The initial development of the LRR along the FFRG and subsequent elongation of the LRR via deformation suggests that the hydrometeors

within the ribbon may originate on the north side of the supercell updraft.

In addition to deformation, the evolution of ζ and vertical velocity within the most pronounced LRRs is of interest. At 2142 UTC, LRR A is the widest of all the analyzed LRRs in this study (Fig. 12a). LRR A is also associated with the largest mean cyclonic ζ above 2 km (Fig. 12c). Below 2 km, the mean vertical vorticity observed within the ribbon is marginally anticyclonic. LRR A is associated with upward motion throughout its depth (Fig. 12c); however, we caution interpretation of the sign of vertical velocity in the lowest 1–2 km because the magnitudes of vertical velocity are small and within the uncertainty of the analysis. By 2146 UTC, LRR A has decayed significantly and is no longer the most apparent LRR within the supercell (Fig. 12b). Matured LRR B is now collocated with the remnants of LRR A along its southern extent. LRR B exhibits increasing mean upward motion with height and mean cyclonic ζ above 2 km, similar to LRR A during its mature stage (Fig. 12d).

By 2152 UTC, LRR B has narrowed and translated rearward within the supercell, and it exhibits smaller deficits in Z_H , compared to 2146 UTC (Fig. 13a). The mean vertical motion within LRR B is still directed upward but is smaller in magnitude at almost every level (Fig. 13c). LRR B no longer exhibits cyclonic ζ above 3 km; however, the lower bound of mean cyclonic ζ within the ribbon has descended to 1 km. By 2154 UTC, LRR C has translated rearward and has begun merging with LRR B (Fig. 13b). At this time, the combined ribbons (B + C) exhibit increased cyclonic ζ above 2 km (Fig. 13d). Additionally, the merging ribbons have a greater deficit in Z_H , causing LRR B + C to be more visible than either ribbon

⁶ It is necessary to assume that the precipitation type and intensity within the LRR are approximately steady state for short time scales for the precipitation to be deformed as it descends through the vertically extensive (1–2 km) deforming airflow.

⁷ The axes of dilatation were calculated using Cohen and Schultz (2005)'s Eq. (7), with Fig. 11 modeled after Bluestein (1977).

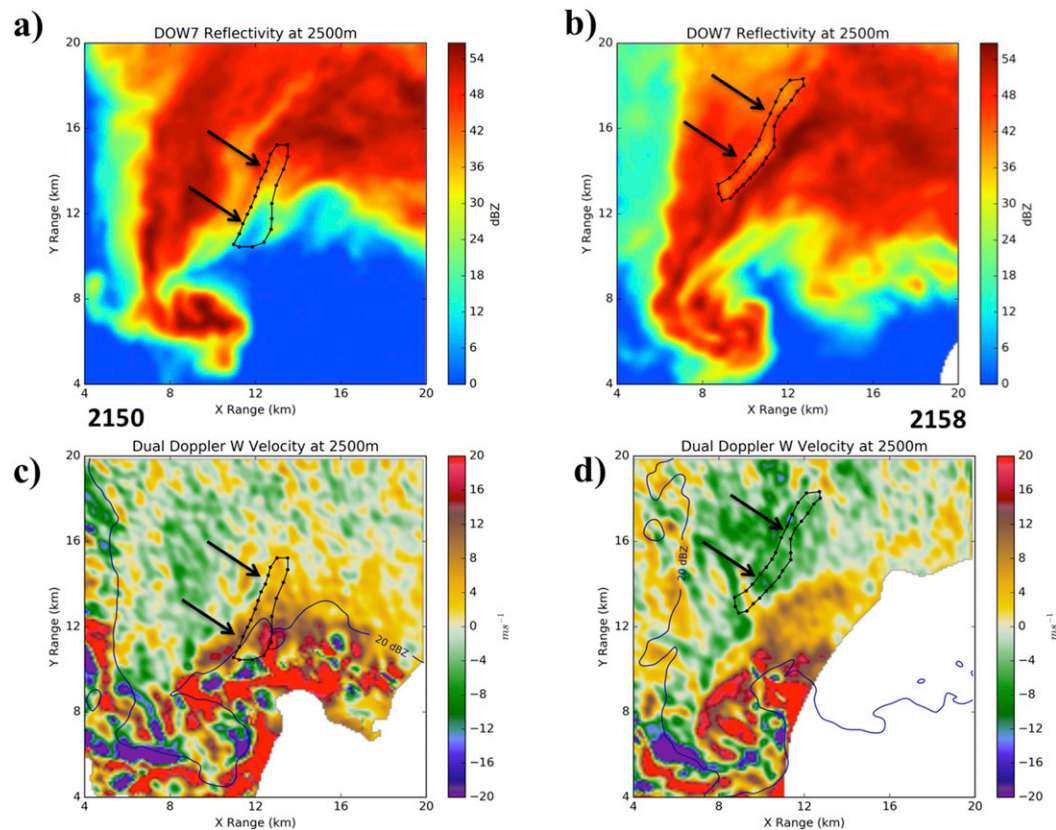


FIG. 9. (a),(b) Objectively analyzed DOW7 reflectivity (shaded; dBZ) and (c),(d) dual-Doppler-derived vertical velocity (shaded; m s^{-1}) with contours of reflectivity overlaid on the 5 Jun 2009 Goshen County, WY, supercell at (a),(c) 2150 and (b),(d) 2158 UTC for 2500 m ARL. Black boundaries indicate the position of the LRR, and the blue lines represent the 20-dBZ DOW7 reflectivity contour.

was at 2152 UTC. The magnitude of mean vertical velocity within the merging ribbons decreases slightly in the highest analyzed levels, but otherwise, changes from the previous time are minimal.

At 2158 UTC, the region of reduced Z_H associated with LRR B + C disconnects from the FFRG of the supercell (Fig. 14a). It can be seen in the vertical profile of LRR B + C that the low levels ($\sim 500\text{--}1500\text{ m}$) exhibit slightly downward mean vertical motion, and the near-surface levels have weak mean cyclonic ζ (Fig. 14c). LRR B + C exhibits slightly larger mean cyclonic ζ above 2.5 km, compared to previous times. Mean vertical motion below 3 km has become directed downward for the first time. By 2200 UTC, LRR B + C has decayed to the point where it is nearly indistinguishable from its surroundings in the upper levels (Fig. 14b); however, it can still be seen in the lower levels (not shown). LRR B + C now exhibits downward vertical velocity throughout the analyzed depth. It can be seen in later dual-Doppler analyses (not shown) that LRR B + C quickly decays after the presented analysis period, and a new dominant LRR develops in a region similar

to where LRRs B and C formed. However, the close proximity of the radars to the LRR precludes dual-Doppler analyses above $\sim 1.5\text{ km}$ for this later analysis time.

In general, it is noted that above $\sim 2\text{ km}$, the LRRs in the Goshen County storm were associated with upward mean vertical motion and mean cyclonic ζ . The strongest ζ occurred early in their life cycles, while they were closest to the FFRG. As the LRRs translated rearward within the supercell and filled in Z_H , the cyclonic ζ within them weakened, perhaps becoming anticyclonic, and the direction of vertical motion reversed.⁸ The combination of cyclonic mean ζ and upward mean vertical motion within

⁸ Decreasing vorticity within the LRR throughout its decay may contribute to the changing sign of vertical velocity through its contribution to nonlinear dynamic perturbation pressure. However, without knowledge of the vertical buoyancy distribution and the linear term of dynamic perturbation pressure, the relative importance of nonlinear dynamic perturbation pressure to vertical velocity tendency cannot be estimated.

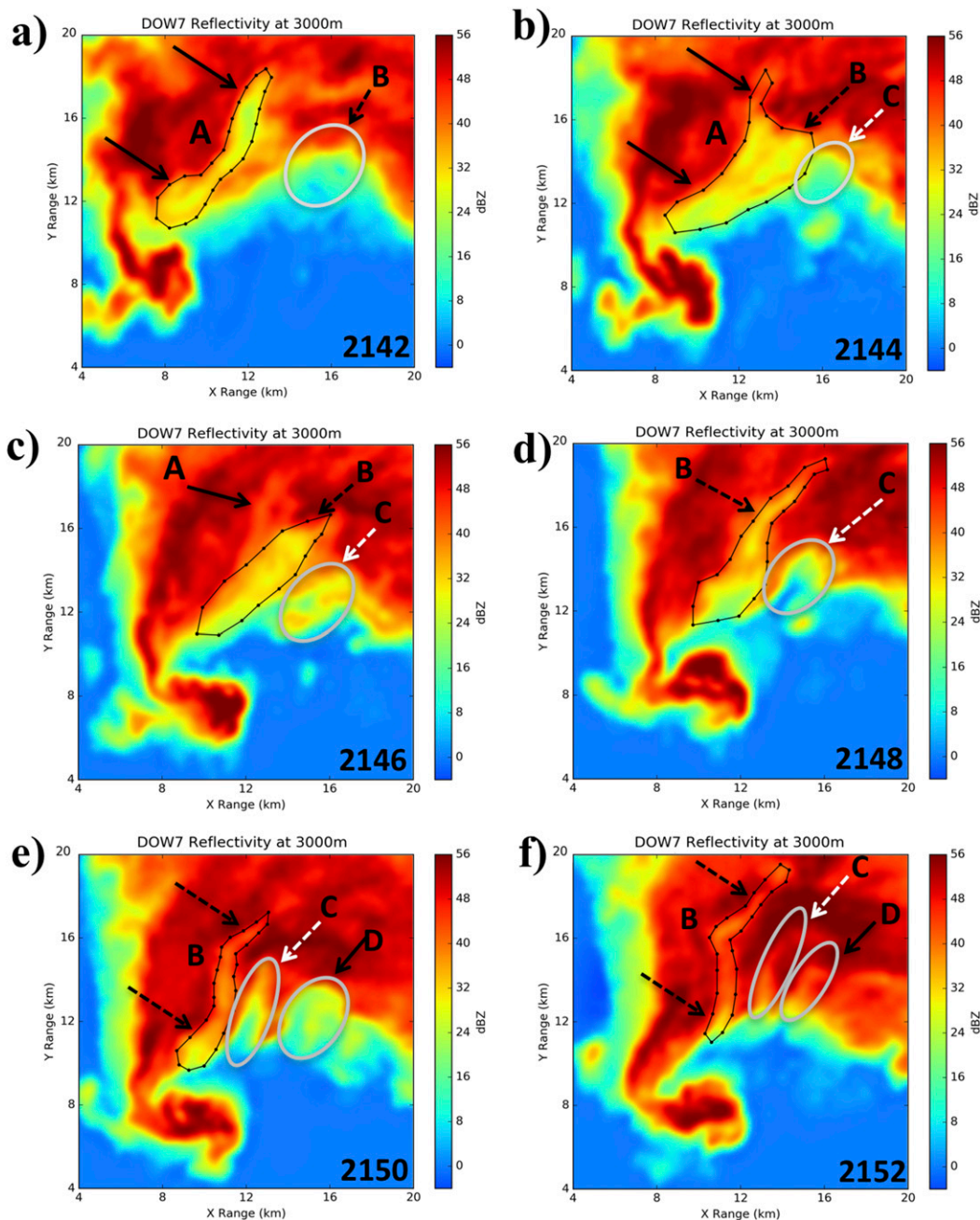


FIG. 10. Objectively analyzed DOW7 reflectivity at 3000 m (shaded; dBZ) valid at (a) 2142, (b) 2144, (c) 2146, (d) 2148, (e) 2150, and (f) 2152 UTC. Black boundaries indicate the positions of the mature LRRs, and ovals indicate the positions of developing LRRs.

developing LRRs, both of which steadily decay through the life cycle of the ribbon, may indicate that most of the development of an LRR occurs along the FFRG. The mature stage of the LRR is characterized by a deformed region of reduced Z_H moving to the rear flank of the supercell prior to the LRR completing its decay.

c. *Polarimetric observations from the 5 June 2009 Goshen County, Wyoming, supercell*

1) CORRELATION COEFFICIENT

In addition to deficits in Z_H and Z_{DR} noted in Wurman et al. (2012) and Kosiba et al. (2013), Snyder et al. (2013) note that a deficit in ρ_{HV} is sometimes

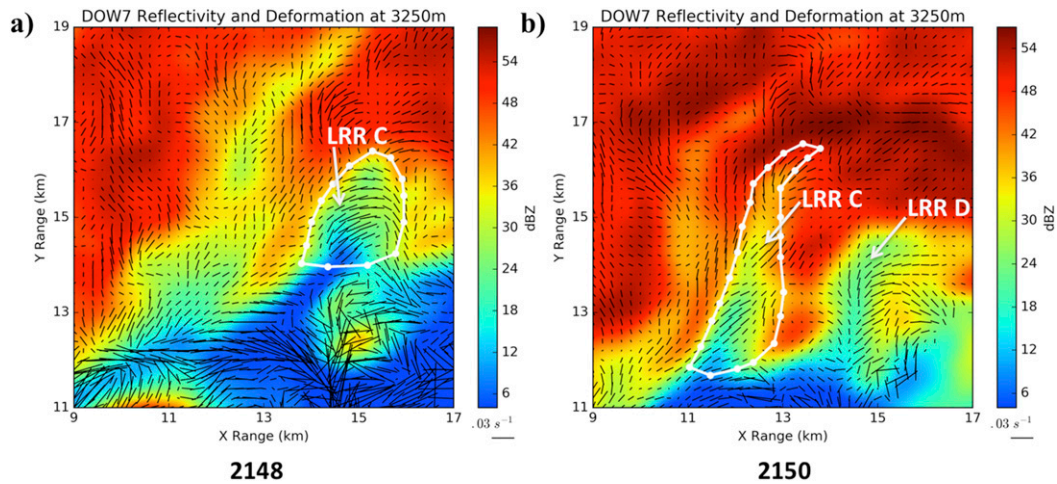


FIG. 11. Objectively analyzed DOW7 reflectivity (shaded; dBZ) and dual-Doppler-derived axes of deformation (lines; s^{-1}) at (a) 2148 and (b) 2150 UTC. White boundaries indicate the position of LRR C.

associated with the LRR. At least one instance of the LRR in this study displays an increasing and more defined deficit in ρ_{hv} with height (Fig. 15). Values of ρ_{hv} within this particular LRR are as low as 0.4 in both the 6°

and 8° scans (Figs. 15c,f). While ρ_{hv} of 0.4 are typically low for most hydrometeors, there are previous observations of hail exhibiting similar values of ρ_{hv} at X-band (e.g., Schwarz and Burgess 2011; Snyder et al. 2013). At

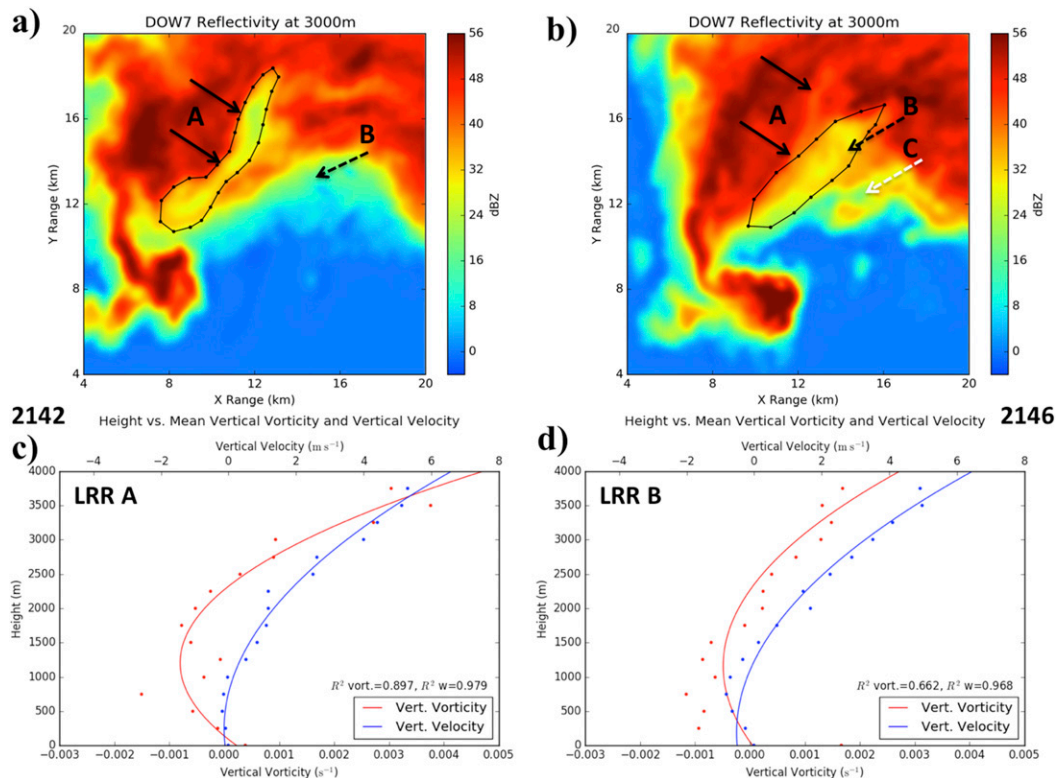


FIG. 12. (a),(b) Objectively analyzed DOW7 reflectivity (dBZ) and (c),(d) plots of mean vertical vorticity (red lines; s^{-1}) and mean vertical velocity (blue lines; $m s^{-1}$) vs height at (a),(c) 2142 and (b),(d) 2146 UTC for all grid points inside of LRR A and LRR B, respectively. A second-order best-fit line is overlaid on the data points. Arrows indicate the position of mature LRR A and developing LRRs B and C.

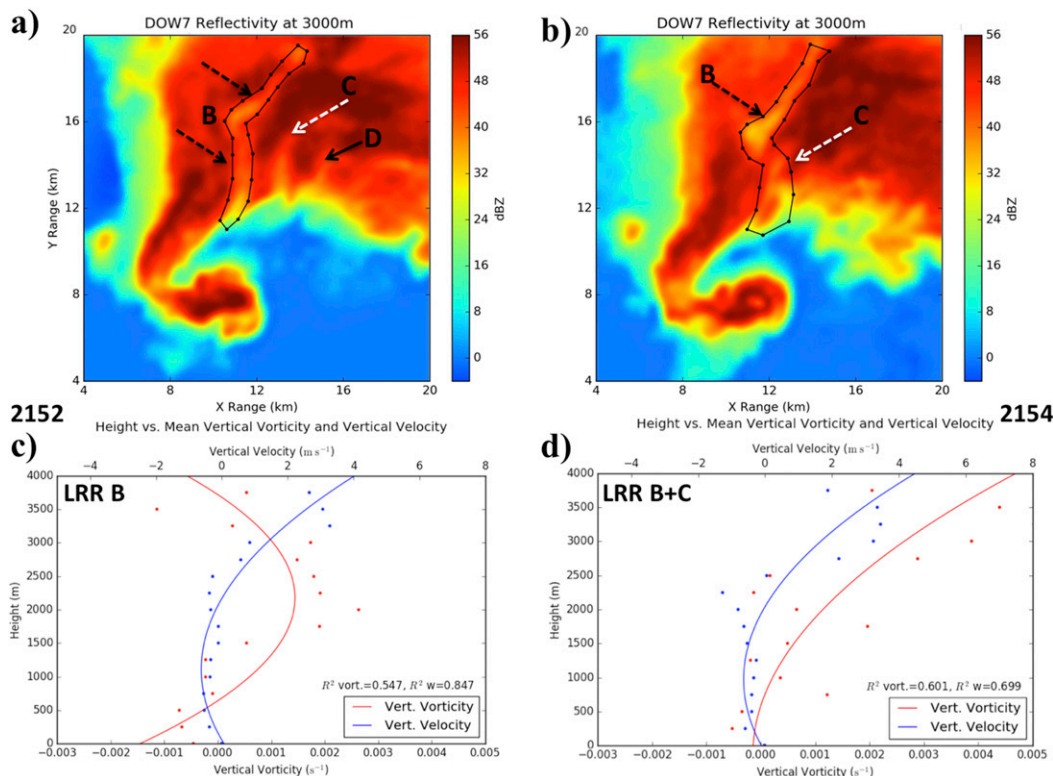


FIG. 13. As in Fig. 12, but at (a),(c) 2152 and (b),(d) 2154 UTC with vertical plots for LRR B and merging LRRs B + C, respectively. The arrows indicate the position of decaying LRR B and maturing LRRs C and D.

both elevations, the LRR is observed above the melting layer. Thus, ρ_{hv} may have an advantage over Z_{DR} in identifying the LRR in the presence of ice hydrometeors, which exhibit Z_{DR} values similar to the ribbon.

Investigation of higher elevation scans for this case reveals a relatively smooth transition into an east–west-oriented, oval region of decreased ρ_{hv} collocated with locally enhanced Z_{DR} (Fig. 16). An outer ring of enhanced Z_{DR} also exists, highlighted by a circle in Fig. 16. These regions are similar to those described by Kumjian and Ryzhkov (2008). We can infer the presence of an updraft in this region from the Z_{DR} ring and the mesocyclone observed Doppler velocity (Fig. 16b) and from radial convergence and the implied presence of Z_{DR} columns (e.g., Kumjian et al. 2014). Dual-Doppler analyses from 10 min prior to this time (not shown) confirm strong upward motion in the low levels (~1–2 km) collocated with these features, but the presence of updrafts at higher altitudes cannot be confirmed due to a lack of dual-Doppler coverage. In addition to illustrating a Z_{DR} ring, Fig. 16 exhibits the upper levels (~5 km) of an LRR. A narrow ribbon of decreased Z_H associated with the LRR is visible. It is noted that the southwest portion of the ribbon appears to curve to the west. Additionally, it appears that the LRR parallels a region of radial

convergence aloft, like what was noted by Snyder et al. (2013).

2) DIFFERENTIAL PHASE

The LRR is found at a range where Φ_{DP} is locally minimized (Fig. 17). The nonmonotonic behavior of Φ_{DP} in the vicinity of the LRR indicates that significant contributions to Φ_{DP} from backscatter differential phase may be occurring within the LRR (Trömel et al. 2013). This would suggest that nonspherical hydrometeors within the LRR are electrometrically large (relative to the wavelength of UMass X-Pol) and that resonance scattering is occurring. Across the central axis of the LRR, Φ_{DP} is relatively constant with radial distance in most cross sections.

Beyond the range of the LRR, Φ_{DP} increases more monotonically, implying positive K_{DP} , similar to what Romine et al. (2008) described as the “ K_{DP} foot” in the 8 May 2003 Oklahoma City supercell. Romine et al. (2008) note that large hail was observed at mesonet stations coinciding with the passage of the leading edge of the K_{DP} foot. This region is very similar in location to the position of the LRR in the Goshen County supercell, and hail could potentially explain the observed gradient in backscatter differential phase. The addition of these

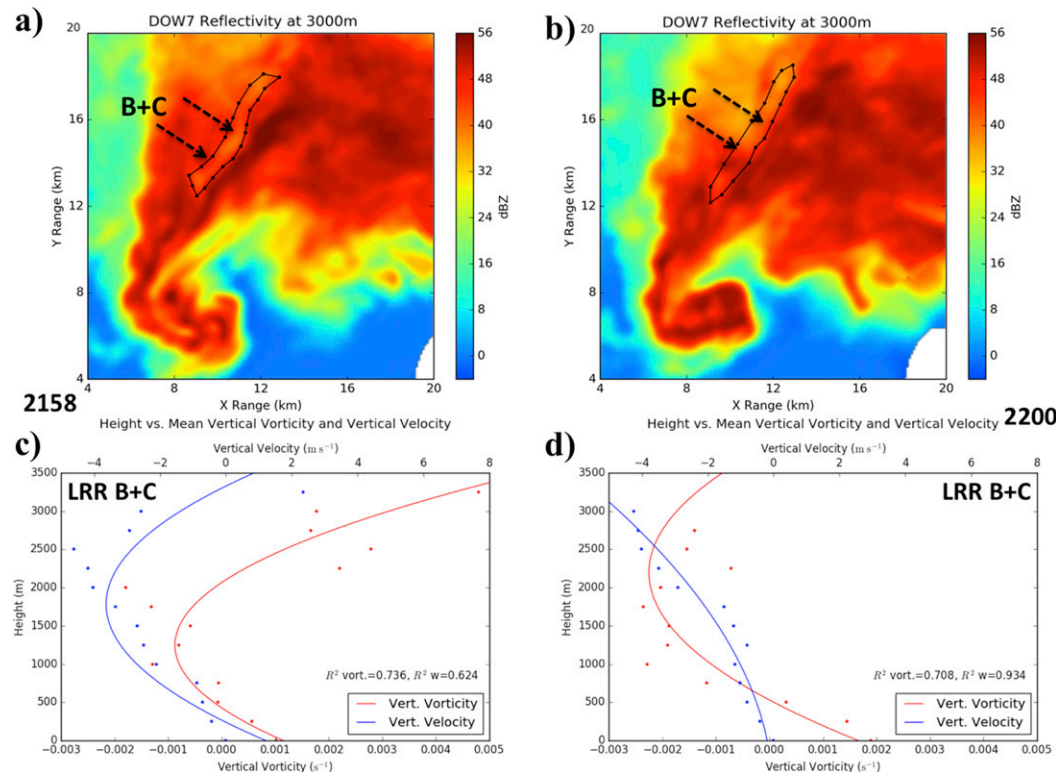


FIG. 14. As in Fig. 12, but at (a),(c) 2158 and (b),(d) 2200 UTC for 2500 m ARL with vertical plots for merged LRR B + C. The arrows indicate the position of merged LRR B + C.

observations to previous ones by Snyder et al. (2013) may allow some conjectures to be made regarding the microphysical composition of the LRR, which will be the topic of discussion of the next section.

4. Discussion

a. Inferred microphysical composition of observed LRRs

It is seen in vertically stacked objective analyses of DOW7 reflectivity that the deficit in Z_H associated with the LRRs examined herein disappears aloft before disappearing at low levels, consistent with possible downward dissipation of this feature (Fig. 18). At 2158 UTC 5 June 2009, the LRR is apparent at 1 and 2 km but is only faintly visible at 3 km (Fig. 18a). By 2200 UTC, the LRR is more visible at 1 km but exhibits little or no reflectivity deficit at either 2 or 3 km (Fig. 18b). The “filling” in reflectivity is most significant at 2 km, where all evidence of the LRR in the southern portion of the left flank disappears entirely, leaving only possible remnants farther north. Similar remnants may also exist at 3 km but are separate from where the LRR is most apparent in the low levels. This particular LRR persists in the low levels for ~ 4 min before disappearing altogether (not shown),

eliminating the possibility of the apparent decay being a result of the time elapsed in completing the radar volume.

The decay of the LRR is possibly due to the fallout of hydrometeors within the ribbon. Two possible hydrometeor regimes could potentially explain the radar representation. The first possibility is that relatively small liquid hydrometeors dominate the particle size distributions (PSDs) within the LRR, as hypothesized by Wurman et al. (2012). Small raindrops would exhibit reduced Z_{DR} and relatively modest Z_H . In this case, the lower ρ_{hv} within the LRR would be attributed to a volume of mixed-phase hydrometeors above the melting layer (e.g., Straka et al. 2000) because the observed signal-to-noise ratio is not significantly reduced within the ribbon (not shown). However, extremely low ρ_{hv} and evidence of significant gradients in backscatter differential phase near the LRR (as can be inferred from Fig. 17) do not support the hypothesis that small raindrops solely comprise the LRR.

The second possible dominant hydrometeor type is large hail ($\gg 1$ cm in diameter) with Z_{DR} near 0 dB (Kumjian and Ryzhkov 2008). The correlation coefficient within regions of large hail can be significantly reduced owing to resonance effects; the reduction in ρ_{hv} can also be seen where hail and liquid drops (such as those shed from melting hail) coexist. However, locally reduced reflectivity

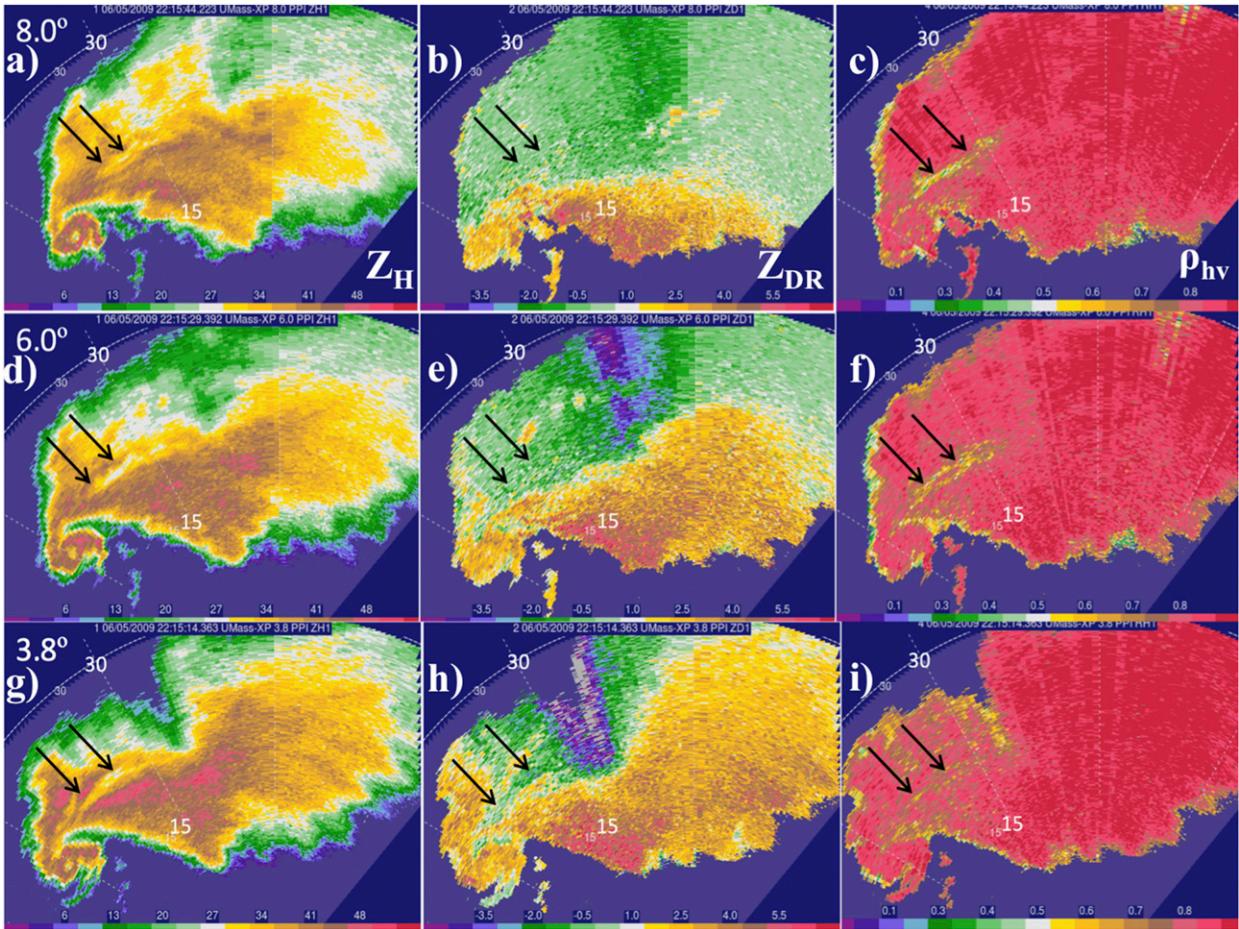


FIG. 15. PPIs of UMass X-Pol (a),(d),(g) reflectivity (dBZ); (b),(e),(h) differential reflectivity (dB); and (c),(f),(i) correlation coefficient at (a)–(c) 8.0°, (d)–(f) 6.0°, and (g)–(i) 3.8° collected on 5 Jun 2009 that illustrate the vertical structure of an LRR. Arrows indicate the position of the LRR. Reference distances (km) are labeled in white.

would only be possible if destructive interference within the Mie scattering regime occurred, similar to the simulated melting hail shown in Ryzhkov et al. (2013) (their Fig. 8b), or if hail fell in such small concentrations that relatively low power was returned from the volume. Additionally, because of the proximity of the LRR to the FFRG, the size of raindrops not associated with drop shedding may be relatively large (Kumjian and Ryzhkov 2008; Dawson et al. 2014), and thus, the concentration of large drops must be small enough such that hail dominated the total backscattered signal to keep the net Z_{DR} low within the radar volumes sampling the LRR(s).

Observations of large hail within regions characterized by relatively low reflectivity are not without precedent at S band (Kumjian et al. 2010; Picca and Ryzhkov 2012; Snyder et al. 2014). Moreover, large hail is likely to exhibit lower reflectivity at X band, compared to what is often observed at S band (e.g., Snyder et al. 2010). Kumjian et al. (2010) hypothesized that the

largest hail may fall near the updraft and at the periphery of the largest reflectivity echoes. This would occur because of the minimal horizontal advection that occurs for particles with large fall speeds. Additionally, the number concentration of the largest hailstones is rather small because there are only a select few hailstones that interact with the updraft in the optimal locations (Nelson 1983). Kumjian et al. (2010) note instances of very large hail falling in low concentrations and in the absence of any other precipitation. Regions of hail similar to those described by Kumjian et al. (2010) would exhibit very similar characteristics to those observed within the LRR, including a deficit in Z_H due to reduced backscattered power that would occur if the hail fell in low concentrations.

Both proposed PSDs within the LRR could potentially help explain the deficits in θ_{ep} observed within the LRR. Phase changes associated with the melting of hail and the evaporation of small drops would both reduce

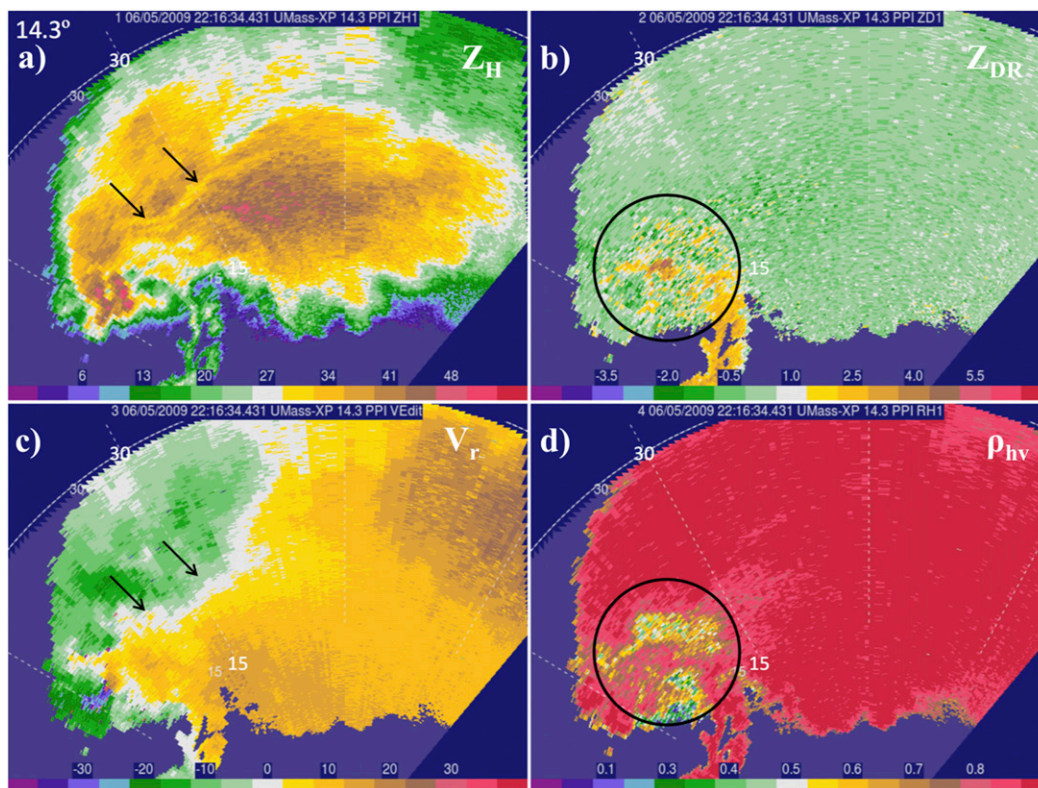


FIG. 16. PPIs of UMass X-Pol (a) reflectivity (dBZ), (b) differential reflectivity (dB), (c) radial velocity (m s^{-1}), and (d) correlation coefficient at 14.3° ($\sim 4\text{--}5$ km ARL at the range of the $Z_{\text{DR}}/\rho_{\text{hv}}$ ring) collected on 5 Jun 2009 that illustrate the upper levels of the LRR (arrows) and a Z_{DR} ring (circled). Reference distances (km) are labeled in white.

the θ_{ep} of parcels within the LRR. If evaporative cooling or melting were enhanced within the LRR, compared to surrounding regions, a local deficit in θ_{ep} would be expected. In the case of large hail, any drops that shed from melting would likely be relatively small (Rasmussen et al. 1984), especially in comparison to large drops present elsewhere along the FFRG associated with storm-scale size sorting. Therefore, the shed drops would be more easily evaporated than drops outside the LRR and may have larger evaporative cooling potential.

Observations of changes in Φ_{DP} owing to gradients in backscatter differential phase within the ribbon by Snyder et al. (2013), as well as in this study, might also suggest the occurrence of resonance scattering, which would support the theory that large scatterers, like hail, exist in the ribbon. Additionally, nonzero backscatter differential phase would rule out spherical particles, such as small raindrops (e.g., Trömel et al. 2013).

b. Vertical motions within the LRR

It can be seen in dual-Doppler analyses of the Goshen supercell that LRRs exhibit upward vertical motion for

much of their life cycles (e.g., Fig. 9c). However, as they decay, LRRs exhibit downward vertical motion (e.g., Fig. 9d). Thus, it is important to determine at which point during the life cycle of the LRR that the StickNet probes sample the ribbon in each case to determine whether parcel source region may explain the minimum in θ_{ep} observed within the ribbon.

The StickNet array sample of one of the Goshen LRRs occurred at 2225 UTC, 15 min after the end of the dual-Doppler analysis performed (see Fig. 20). At 2223 UTC, an LRR resides just to the west of the position of StickNet probe 102b in the left flank of the supercell, a region where previous LRRs decayed within this storm. By 2225 UTC, the supercell has translated to the east, and the StickNet probe samples a minimum in θ_{ep} (Fig. 19b). However, the LRR from the previous time has almost decayed entirely, being partially replaced with a region of high Z_{H} . A second LRR develops well to the east of the probe at this time. The concurrent presence of these two ribbons is clear in the 4.8° scan (Fig. 19c). At lower scans, only the decaying LRR is visible, and at higher scans, only the developing LRR is visible, hinting to the top-down decay that appears

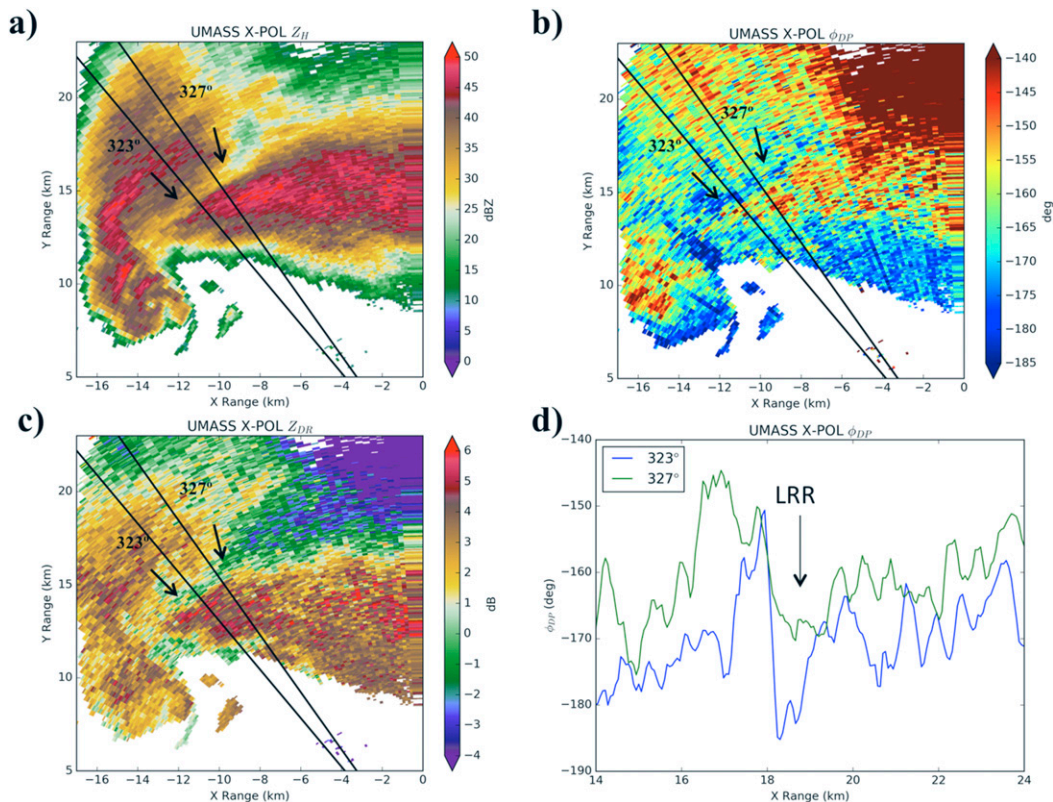


FIG. 17. PPIs of UMass X-Pol (a) reflectivity (shaded; dBZ), (b) differential phase (shaded; °) and (c) differential reflectivity (shaded; dB), and (d) radial profiles of differential phase (°) at 4° elevation for an LRR centered at a range of approximately 19 km collected at 2221 UTC 5 Jun 2009. Arrows indicate the position of the ribbon in each panel, and the black lines in (a)–(c) indicate the position of the 323° and 327° radials plotted in (d).

to be consistent in all of the LRRs used for this study. The relative position of the decaying LRR to the StickNet probe at 2223 and 2225 UTC suggest that the minimum in θ_{ep} sampled by the probe is more likely to be associated with the decaying ribbon than the developing ribbon.

The 18 May 2010 supercell near Dumas, Texas, produced multiple LRRs, including simultaneous parallel LRRs observed at 2328 UTC (Fig. 20). The two ribbons rotate counterclockwise, merge, and move westward, in a storm-relative sense, into the rear flank of the

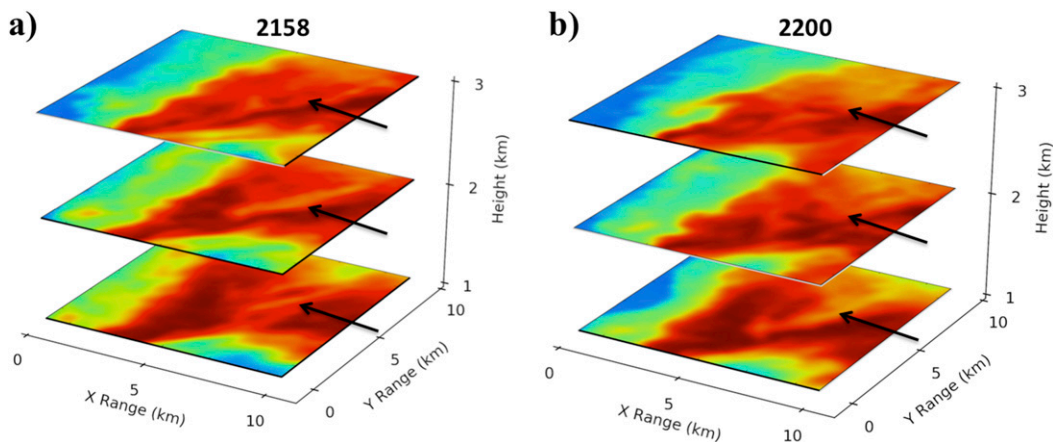


FIG. 18. Stacked CAPPIs of DOW7 reflectivity (shaded; dBZ) collected on 5 Jun 2009 at (a) 2158 and (b) 2200 UTC. Arrows indicate the position of the LRR.

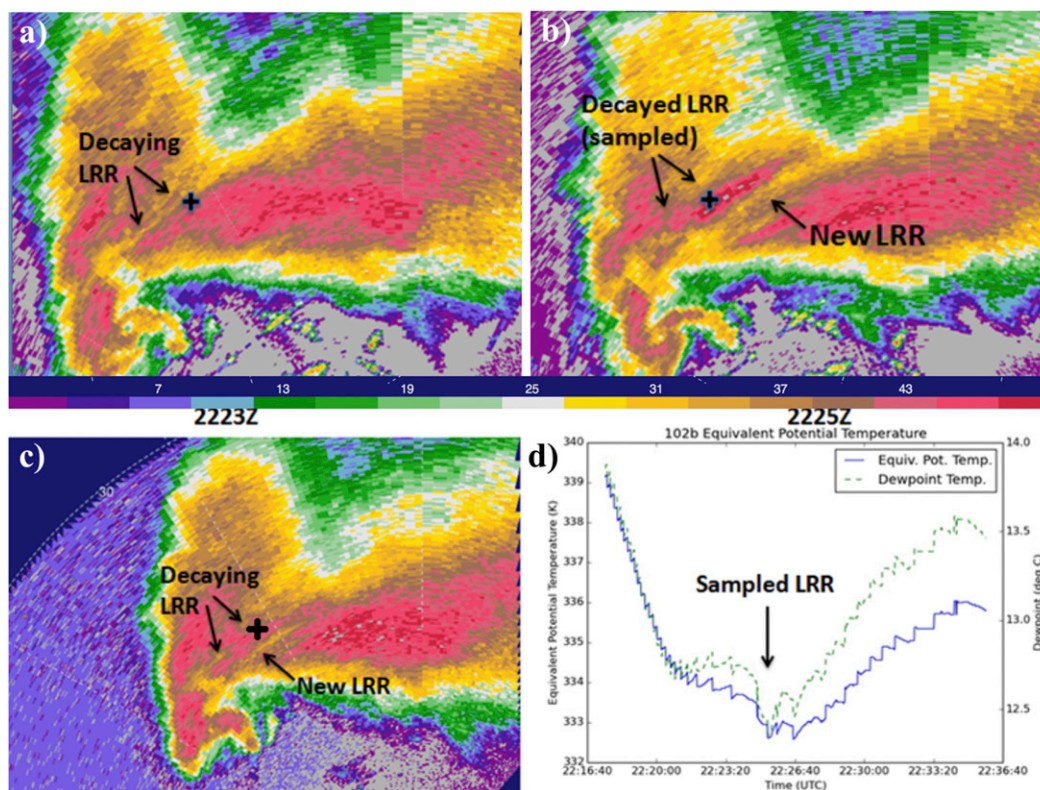


FIG. 19. PPIs of UMass X-Pol reflectivity at (a),(c) 2223 and (b) 2225 UTC at (a),(b) 2.8° and (c) 4.8° that exhibit developing and decaying LRRs. Also shown is (d) a time series of pseudoequivalent potential temperature (blue trace; K) and Td (green trace; °C) taken by StickNet probe 102b on 5 Jun 2009. Arrows indicate the position of the LRR, and plus signs indicate the position of probe 102b.

supercell and are sampled by an array of StickNet probes at 2336 UTC. There are no other apparent LRRs within the storm at this time, and the 2336 UTC scan of Z_{DR} places the probe directly inside the ribbon collocated with the minimum in θ_{ep} . By 2338 UTC, the sampled LRR decays and is only a diffuse feature in Z_{DR} . The LRR is no longer visible in any field after this time. Thus, it can be concluded that the minimum in θ_{ep} sampled by the StickNet probes was also associated with a decaying ribbon in this case. The 10–11 June 2010 supercell near Last Chance, Colorado, produced the last LRR used for this study. Two simultaneous LRRs, at different stages in their life cycles, are in close proximity to the StickNet array at the time when a minimum in θ_{ep} was sampled (not shown), which makes determining which LRR was responsible for the thermodynamic signature difficult. However, a concurrently sampled divergent wind pattern (not shown) suggests that a downdraft associated with the decaying LRR is most likely concurrent with the minimum in θ_{ep} .

Because the StickNet samples in this study are predominately of decaying LRRs, it is plausible that source

regions high within the supercell and associated downward vertical motion within decaying LRRs may be responsible for the minimum in θ_{ep} observed within an LRR. If this is the case, then it is possible that an LRR in its developing or mature stage may not exhibit locally reduced θ_{ep} at the surface due to its location in a region characterized by upward vertical motion. However, if, as previously mentioned, phase changes of particles within the LRR significantly contribute to the minimum in θ_{ep} , the LRR would likely exhibit a local deficit in θ_{ep} , regardless of when it is sampled.

5. Conclusions

This project extends the initial work done by Snyder et al. (2013) on characterizing the inferred microphysical properties of observed LRRs to include the evolution and vertical distribution of radar moments, in addition to providing the first surface thermodynamic and dual-Doppler-derived kinematic analyses of the LRR. It can be seen from the surface observations that LRRs are associated with a local minimum in θ_{ep} across multiple cases.

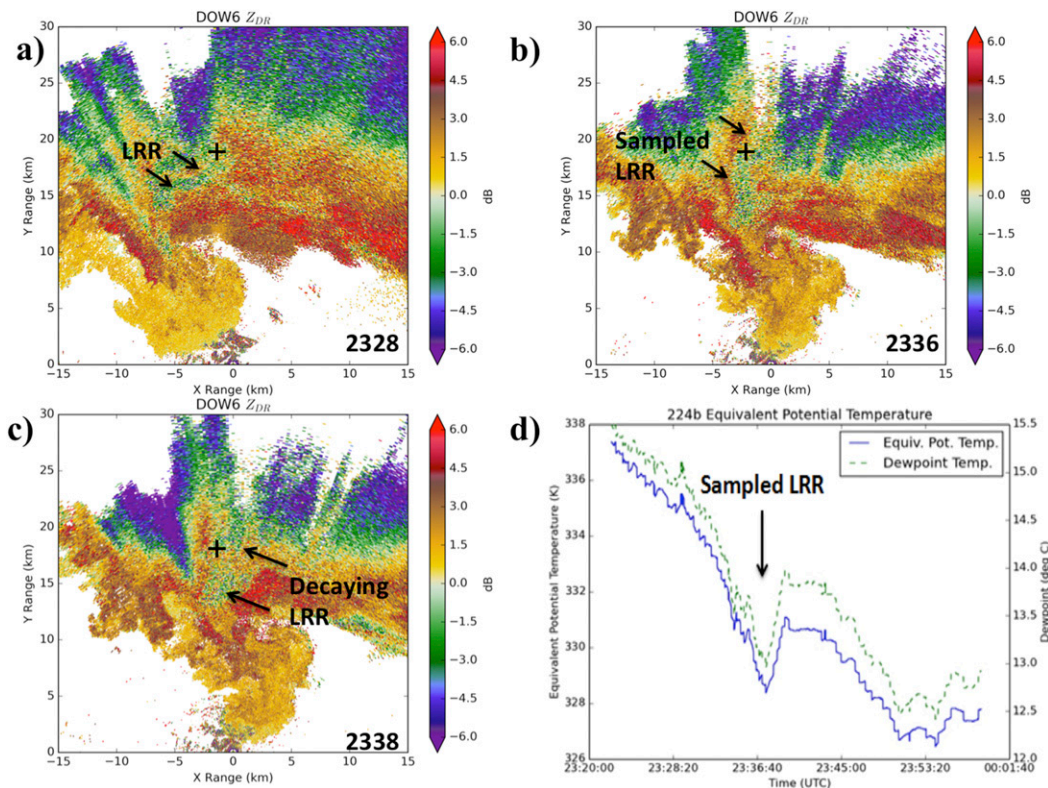


FIG. 20. PPIs of DOW6 differential reflectivity (dB) at (a) 2328, (b) 2336, and (c) 2338 UTC at 3.0° that exhibit developing and decaying LRRs. Also pictured is (d) a time series of pseudoequivalent potential temperature (blue trace; K) and Td (green trace; °C) taken by StickNet probe 224b on 18 May 2010. Arrows indicate the position of the LRR, and plus signs indicate the position of probe 224b.

In the cases examined so far, it seems that there is a general pattern in the evolution of the observed LRRs:

- (i) The LRR first manifests as a notch in Z_H along the FFRG of the supercell (Fig. 21). This region is characterized by locally enhanced deformation where the local axes of dilatation largely parallel the axis of the Z_H notch.
- (ii) The transition from a developing LRR into a mature LRR involves the elongation of the Z_H deficit while the LRR translates farther rearward within the supercell. Developing and mature LRRs are associated with mean cyclonic ζ and upward vertical velocity above 2 km.
- (iii) As the LRR translates farther into the left flank of the supercell, it begins to decay. The deficit in Z_H within the ribbon becomes smaller, and the width of the LRR narrows until it disappears entirely from top to bottom within the analyzed 4-km column. The region of reduced Z_H may also disconnect from the FFRG of the supercell during the late stages. During its decay, the LRR no longer exhibits cyclonic ζ , and vertical velocity becomes

directed downward. At this point during the decay, the LRR exhibits a local minimum in θ_{ep} , as measured by arrays of StickNet probes at the surface.

The LRR dissipates from the top down, which suggests that hydrometeor fallout may drive the microphysical representation in the radar fields. The ribbon exhibits reduced Z_H and Z_{DR} , which implies a PSD composed of either small liquid hydrometeors or small concentrations of hail mixed with small drops. Intermittent observations of very low ρ_{hv} and nonzero backscatter differential phase within the LRR, as well as the position of the LRR relative to the primary updraft, favors the hypothesis of sparse, large hail within the LRR; however, this study did not have the observations to confirm that hail occurred. Therefore, future research should focus on identifying the types of hydrometeors through means of ground verification or a robust hydrometeor classification. Comparisons of polarimetric radar observations at multiple wavelengths (e.g., Picca and Ryzhkov 2012) would also be useful for estimating the size of hydrometeors within the LRR. Additional future research should also determine what mechanisms

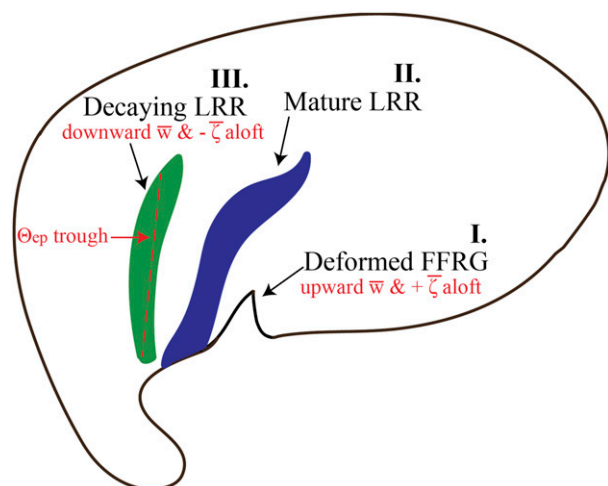


FIG. 21. A schematic of the life cycle of the LRR aloft (>2 km) from its (i) genesis as a deformation of the FFRG, into (ii) a mature LRR (blue), and finally (iii) into the rear flank where it decays (green).

are driving the upward vertical motion within the LRR; why the hydrometeors that characterize the ribbon are confined to such a concentrated region; and what effect, if any, the presence of an LRR has on the buoyancy of nearby parcels and the vorticity budget of the parent supercell.

Acknowledgments. This work was supported by National Science Foundation (NSF) Grants AGS-0800542, AGS-0948492, AGS-0964088, AGS-1262048, and AGS-1447268. Casey B. Griffin was supported in part by the AMS 21st Century Campaign's graduate fellowship. Funding for Jeffrey Snyder was provided by NOAA/Office of Oceanic and Atmospheric Research under NOAA–University of Oklahoma Cooperative Agreement NA11OAR4320072, U.S. Department of Commerce. The DOW facility is supported by NSF Grants AGS-0734001 and AGS-1361237. VORTEX2 logistics were supported by NSF Grant AGS-0724318. The authors thank Eric Bruning and Johannes Dahl for their help in improving this work as a part of the lead author's master's thesis at TTU. The authors also thank Zach Weinhoff for scientific conversation. We thank the students and faculty from the TTU Atmospheric Science Group; the TTU National Wind Institute; the University of Michigan Atmospheric, Oceanic, and Space Science program; the University of Oklahoma (UMass X-Pol); and the Center for Severe Weather Research (DOWs) for their dedicated efforts in the field. Finally, the authors thank the three anonymous reviewers whose suggestions greatly improved this work.

REFERENCES

- Barnes, S., 1964: A technique for maximizing details in numerical weather map analysis. *J. Appl. Meteor.*, **3**, 396–409, [https://doi.org/10.1175/1520-0450\(1964\)003<0396:ATFMDI>2.0.CO;2](https://doi.org/10.1175/1520-0450(1964)003<0396:ATFMDI>2.0.CO;2).
- , 1973: Mesoscale objective map analysis using weighted time-series observations. NOAA Tech. Memo. ERL NSSL-62, 60 pp.
- Bluestein, H., 1977: Synoptic-scale deformation and tropical cloud bands. *J. Atmos. Sci.*, **34**, 891–900, [https://doi.org/10.1175/1520-0469\(1977\)034<0891:SSDATC>2.0.CO;2](https://doi.org/10.1175/1520-0469(1977)034<0891:SSDATC>2.0.CO;2).
- Bolton, D., 1980: The computation of equivalent potential temperature. *Mon. Wea. Rev.*, **108**, 1046–1053, [https://doi.org/10.1175/1520-0493\(1980\)108<1046:TCOEPT>2.0.CO;2](https://doi.org/10.1175/1520-0493(1980)108<1046:TCOEPT>2.0.CO;2).
- Cohen, R. A., and D. M. Schultz, 2005: Contraction rate and its relationship to frontogenesis, the Lyapunov exponent, fluid trapping, and airstream boundaries. *Mon. Wea. Rev.*, **133**, 1353–1369, <https://doi.org/10.1175/MWR2922.1>.
- Dahl, J., M. Parker, and L. Wicker, 2014: Imported and storm-generated near-ground vertical vorticity in a simulated supercell. *J. Atmos. Sci.*, **71**, 3027–3051, <https://doi.org/10.1175/JAS-D-13-0123.1>.
- Dawson, D., E. R. Mansell, Y. Jung, L. Wicker, M. Kumjian, and M. Xue, 2014: Low-level Z_{DR} signatures in supercell forward flanks: The role of size sorting and melting of hail. *J. Atmos. Sci.*, **71**, 276–299, <https://doi.org/10.1175/JAS-D-13-0118.1>.
- Helmus, J., and S. Collis, 2016: The Python ARM Radar Toolkit (Py-ART), a library for working with weather radar data in the Python programming language. *J. Open Res. Software*, **4**, e25, <https://doi.org/10.5334/jors.119>.
- Joss, J., and A. Waldvogel, 1970: Raindrop size distribution and Doppler velocities. Preprints, *14th Conf. on Radar Meteorology*, Tucson, AZ, Amer. Meteor. Soc., 153–156.
- Junyent-Lopez, F., 2003: The design, development, and initial field deployment of an X-band polarimetric Doppler weather radar. M.S. thesis, Dept. of Electrical and Computer Engineering, University of Massachusetts Amherst, 120 pp.
- Koch, S. E., M. desJardins, and P. J. Kocin, 1983: An interactive Barnes objective map analysis scheme for use with satellite and conventional data. *J. Climate Appl. Meteor.*, **22**, 1487–1503, [https://doi.org/10.1175/1520-0450\(1983\)022<1487:AIBOMA>2.0.CO;2](https://doi.org/10.1175/1520-0450(1983)022<1487:AIBOMA>2.0.CO;2).
- Kosiba, K., J. Wurman, Y. Richardson, P. Markowski, P. Robinson, and J. Marquis, 2013: Genesis of the Goshen County, Wyoming, tornado on 5 June 2009 during VORTEX2. *Mon. Wea. Rev.*, **141**, 1157–1181, <https://doi.org/10.1175/MWR-D-12-00056.1>.
- Kumjian, M., and A. Ryzhkov, 2008: Polarimetric signatures in supercells thunderstorms. *J. Appl. Meteor. Climatol.*, **47**, 1940–1961, <https://doi.org/10.1175/2007JAMC1874.1>.
- , J. Picca, S. Ganson, A. Ryzhkov, J. Krause, and A. Khain, 2010: Polarimetric radar characteristics of large hail. *25th Conf. on Severe Local Storms*, Denver, CO, Amer. Meteor. Soc., 11.2, https://ams.confex.com/ams/25SLS/techprogram/paper_176043.htm.
- , A. Khain, N. Benmoshe, E. Ilotoviz, A. Ryzhkov, and V. Phillips, 2014: The anatomy and physics of Z_{DR} columns: Investigating a polarimetric radar signature with a spectral bin microphysical model. *J. Appl. Meteor. Climatol.*, **53**, 1820–1843, <https://doi.org/10.1175/JAMC-D-13-0354.1>.
- Majcen, M., P. Markowski, Y. Richardson, D. Dowell, and J. Wurman, 2008: Multipass objective analyses of Doppler radar data. *J. Atmos. Oceanic Technol.*, **25**, 1845–1858, <https://doi.org/10.1175/2008JTECHA1089.1>.
- Markowski, P., J. Straka, and E. Rasmussen, 2002: Direct surface thermodynamic observations within the rear-flank downdrafts of nontornadic and tornadic supercells. *Mon. Wea. Rev.*, **130**,

- 1692–1721, [https://doi.org/10.1175/1520-0493\(2002\)130<1692:DSTOWT>2.0.CO;2](https://doi.org/10.1175/1520-0493(2002)130<1692:DSTOWT>2.0.CO;2).
- , and Coauthors, 2012a: The pretornadic phase of the Goshen County, Wyoming, supercell of 5 June 2009 intercepted by VORTEX2. Part I: Evolution of kinematic and surface thermodynamic fields. *Mon. Wea. Rev.*, **140**, 2887–2915, <https://doi.org/10.1175/MWR-D-11-00336.1>.
- , and Coauthors, 2012b: The pretornadic phase of the Goshen County, Wyoming, supercell of 5 June 2009 intercepted by VORTEX2. Part II: Intensification of low-level rotation. *Mon. Wea. Rev.*, **140**, 2916–2938, <https://doi.org/10.1175/MWR-D-11-00337.1>.
- Marquis, J., Y. Richardson, P. Markowski, D. Dowell, J. Wurman, K. Kosiba, P. Robinson, and G. Romine, 2014: An investigation of the Goshen County, Wyoming, tornadic supercell of 5 June 2009 using EnKF assimilation of mobile mesonet and radar observations collected during VORTEX2. Part I: Experiment design and verification of the EnKF analyses. *Mon. Wea. Rev.*, **142**, 530–554, <https://doi.org/10.1175/MWR-D-13-00007.1>.
- , —, —, J. Wurman, K. Kosiba, and P. Robinson, 2016: An investigation of the Goshen County, Wyoming, tornadic supercell of 5 June 2009 using EnKF assimilation of mobile mesonet and radar observations. Part II: Mesocyclone-scale processes affecting tornado formation, maintenance, and decay. *Mon. Wea. Rev.*, **144**, 3441–3463, <https://doi.org/10.1175/MWR-D-15-0411.1>.
- Nelson, S., 1983: The influence of storm flow structure on hail growth. *J. Atmos. Sci.*, **40**, 1965–1983, [https://doi.org/10.1175/1520-0469\(1983\)040<1965:TIOSFS>2.0.CO;2](https://doi.org/10.1175/1520-0469(1983)040<1965:TIOSFS>2.0.CO;2).
- Picca, J., and A. Ryzhkov, 2012: A dual-wavelength polarimetric analysis of the 16 May 2010 Oklahoma City extreme hailstorm. *Mon. Wea. Rev.*, **140**, 1385–1403, <https://doi.org/10.1175/MWR-D-11-00112.1>.
- Rasmussen, R., V. Levizzani, and H. Pruppacher, 1984: A wind tunnel and theoretical study on the melting behavior of atmospheric ice particles: III. Experiment and theory for spherical ice particles of radius $> 500 \mu\text{m}$. *J. Atmos. Sci.*, **41**, 381–388, [https://doi.org/10.1175/1520-0469\(1984\)041<0381:AWTATS>2.0.CO;2](https://doi.org/10.1175/1520-0469(1984)041<0381:AWTATS>2.0.CO;2).
- Romine, G., D. Burgess, and R. Wilhelmson, 2008: A dual-polarization-radar-based assessment of the 8 May 2003 Oklahoma City area tornadic supercell. *Mon. Wea. Rev.*, **136**, 2849–2870, <https://doi.org/10.1175/2008MWR2330.1>.
- Ryzhkov, A., M. Kumjian, S. Ganson, and A. Khain, 2013: Polarimetric radar characteristics of melting hail. Part I: Theoretical simulations using spectral microphysical modeling. *J. Appl. Meteor. Climatol.*, **52**, 2849–2870, <https://doi.org/10.1175/JAMC-D-13-073.1>.
- Schroeder, J. L., and C. C. Weiss, 2008: Integrating research and education through measurement and analysis. *Bull. Amer. Meteor. Soc.*, **89**, 793–798, <https://doi.org/10.1175/2008BAMS2287.1>.
- Schwarz, C., and D. Burgess, 2011: Supercell polarimetric signatures at X-band: Data from VORTEX2. *35th Conf. on Radar Meteorology*, Pittsburgh, PA, Amer. Meteor. Soc., 60, <https://ams.confex.com/ams/35Radar/webprogram/Paper191298.html>.
- Skinner, P., C. Weiss, J. Schroeder, L. Wicker, and M. Biggerstaff, 2011: Observations of the surface boundary structure within the 23 May 2007 Perryton, Texas, supercell. *Mon. Wea. Rev.*, **139**, 3730–3749, <https://doi.org/10.1175/MWR-D-10-05078.1>.
- , —, M. French, H. Bluestein, P. Markowski, and Y. Richardson, 2014: VORTEX2 observations of a low-level mesocyclone with multiple internal rear-flank downdraft momentum surges in the 18 May 2010 Dumas, Texas, supercell. *Mon. Wea. Rev.*, **142**, 2935–2960, <https://doi.org/10.1175/MWR-D-13-00240.1>.
- Snyder, J., H. Bluestein, G. Zhang, and S. Frasier, 2010: Attenuation correction and hydrometeor classification of high-resolution, X-band, dual-polarized mobile radar measurements in severe convective storms. *J. Atmos. Oceanic Technol.*, **27**, 1979–2001, <https://doi.org/10.1175/2010JTECHA1356.1>.
- , —, V. Venkatesh, and S. Frasier, 2013: Observations of polarimetric signatures in supercells by an X-band mobile Doppler radar. *Mon. Wea. Rev.*, **141**, 3–29, <https://doi.org/10.1175/MWR-D-12-00068.1>.
- , A. Ryzhkov, H. Bluestein, and S. Blair, 2014: Polarimetric analysis of two giant-hail-producing supercells observed by X-band and S-band radars. *27th Conf. on Severe Local Storms*, Madison, WI, Amer. Meteor. Soc., 166, <https://ams.confex.com/ams/27SLS/webprogram/Paper255455.html>.
- Straka, J., D. Zrnić, and A. Ryzhkov, 2000: Bulk hydrometeor classification and quantification using polarimetric radar data: Synthesis of relations. *J. Appl. Meteor.*, **39**, 1341–1372, [https://doi.org/10.1175/1520-0450\(2000\)039<1341:BHCAQU>2.0.CO;2](https://doi.org/10.1175/1520-0450(2000)039<1341:BHCAQU>2.0.CO;2).
- Taylor, G., 1938: The spectrum of turbulence. *Proc. Roy. Soc. London*, **164**, 476–490, <https://doi.org/10.1098/rspa.1938.0032>.
- Trapp, R., and C. Doswell, 2000: Radar data objective analysis. *J. Atmos. Oceanic Technol.*, **17**, 105–120, [https://doi.org/10.1175/1520-0426\(2000\)017<0105:RDOA>2.0.CO;2](https://doi.org/10.1175/1520-0426(2000)017<0105:RDOA>2.0.CO;2).
- Trömel, S., M. Kumjian, A. Ryzhkov, C. Simmer, and M. Diederich, 2013: Backscatter differential phase—Estimation and variability. *J. Appl. Meteor. Climatol.*, **52**, 2529–2548, <https://doi.org/10.1175/JAMC-D-13-0124.1>.
- Weiss, C. C., and J. L. Schroeder, 2008: StickNet—A new portable, rapidly-deployable, surface observing system. *25th Int. Conf. on Interactive Information Processing Systems for Meteorology, Oceanography, and Hydrology*, New Orleans, LA, Amer. Meteor. Soc., 4A.1, <https://ams.confex.com/ams/pdfpapers/134047.pdf>.
- , D. Dowell, J. Schroeder, P. Skinner, A. Reinhart, P. Markowski, and Y. Richardson, 2015: A comparison of near-surface buoyancy and baroclinity across three VORTEX2 supercell intercepts. *Mon. Wea. Rev.*, **143**, 2736–2753, <https://doi.org/10.1175/MWR-D-14-00307.1>.
- Wurman, J., 2001: The DOW mobile multiple-Doppler network. Preprints, *30th Int. Conf. on Radar Meteorology*, Munich, Germany, Amer. Meteor. Soc., P3.3, https://ams.confex.com/ams/30radar/techprogram/paper_21572.htm.
- , J. Straka, E. Rasmussen, M. Randall, and A. Zahrai, 1997: Design and deployment of a portable, pencil-beam, pulsed, 3-cm Doppler radar. *J. Atmos. Oceanic Technol.*, **14**, 1502–1512, [https://doi.org/10.1175/1520-0426\(1997\)014<1502:DADOAP>2.0.CO;2](https://doi.org/10.1175/1520-0426(1997)014<1502:DADOAP>2.0.CO;2).
- , D. Dowell, Y. Richardson, P. Markowski, E. Rasmussen, D. Burgess, L. Wicker, and H. Bluestein, 2012: The second verification of the origins of rotation in tornadoes experiment: VORTEX2. *Bull. Amer. Meteor. Soc.*, **93**, 1147–1170, <https://doi.org/10.1175/BAMS-D-11-00010.1>.